



EDGEWOOD CHEMICAL BIOLOGICAL CENTER

U.S. ARMY RESEARCH, DEVELOPMENT AND ENGINEERING COMMAND
Aberdeen Proving Ground, MD 21010-5424

ECBC-TR-1478

EVAPORATION AND DEGRADATION OF A SESSILE DROPLET OF VX ON AN IMPERMEABLE SURFACE

Mark J. Varady
Patrick C. Riley
Brent A. Mantooth
Amanda M. Schenning

RESEARCH AND TECHNOLOGY DIRECTORATE

Janet C. Fouse

LEIDOS, INC.
Abingdon, MD 21009-2161

Thomas P. Pearl

DCS CORPORATION
Abingdon, MD 21009-1283

September 2017

Approved for public release: distribution unlimited.



Disclaimer

The findings in this report are not to be construed as an official Department of the Army position unless so designated by other authorizing documents.

Blank

PREFACE

The work described in this report was authorized under project no. CB3062. The work was started in October 2014 and completed in September 2016.

The use of either trade or manufacturers' names in this report does not constitute an official endorsement of any commercial products. This report may not be cited for purposes of advertisement.

This report has been approved for public release.

Acknowledgments

The authors acknowledge the following individuals for their hard work and assistance with the execution of this technical program:

- Michael Roberts and Jerry Glasow (Defense Threat Reduction Agency Joint Science and Technology Office; Fort Belvoir, VA) for support of this program.
- Michelle Sheahy (U.S. Army Edgewood Chemical Biological Center [ECBC]; Aberdeen Proving Ground, MD), Jill Ruth and Brian Luthardt (Leidos, Inc.; Abingdon, MD), and Michael Chesebrough (DCS Corporation; Abingdon, MD), of the Decontamination Sciences Branch for their assistance in the laboratory.
- Barry Williams and Melissa Hulet (Leidos) of the Passive Spectroscopy Branch for assistance with Fourier transform infrared spectroscopy–attenuated total reflection experiments.
- Matt Shue, Larry Procell, and Matthew Willis (ECBC) for providing branch chief level support and technical guidance.

Blank

CONTENTS

1.	INTRODUCTION	1
2.	METHODS AND MATERIALS.....	5
2.1	Chemicals.....	5
2.2	Chromatographic Chemical Analysis	6
2.2.1	High-Purity VX Dose-Confirmation Samples	7
2.2.2	CASARM VX Dose-Confirmation Samples	7
2.2.3	CASARM VX/EMPA Mixtures Dose-Confirmation Samples.....	8
2.3	DCA Experiments.....	8
2.4	Phase-Separation Experiments.....	9
2.5	Infrared Spectroscopy Experiments	9
2.6	Vial Reactor Experiments	9
2.7	Mathematical Models and Simulations.....	10
3.	RESULTS	13
3.1	DCA Results for High-Purity VX.....	14
3.2	DCA Results for Degradation Byproducts	16
3.3	DCA Results for CASARM VX.....	17
3.4	DCA Results for VX/EMPA Mixtures	19
3.5	Contact Angle Results Summary	21
3.6	Phase-Separation Experiments.....	21
3.7	Vial Reactor Experiments under Various Environmental Conditions.....	22
3.8	Summary of Key Experimental Results.....	24
4.	COMPUTATIONAL RESULTS.....	25
4.1	Estimation of Gas-Phase Diffusivities	25
4.2	Estimation of Vapor Pressures.....	26
4.3	Degradation and Evaporation for Fixed Droplet Geometry	28
5.	SUMMARY AND CONCLUSIONS	30
	LITERATURE CITED	33
	ACRONYMS AND ABBREVIATIONS	35
	APPENDIX: AGENT PURITY CERTIFICATES.....	37

FIGURES

1.	Video clip showing VX droplet evolution from 20 to 60 °C.....	2
2.	Schematic of autocatalytic hydrolysis of VX, reproduced from Brevett et al. ³ Solid black lines indicate reaction pathways, and dashed red lines indicate how EMPA, produced during the reaction process, acts as an autocatalytic species.....	3
3.	Fit of kinetic data determined by Brevett et al. to an Arrhenius law. The 22 °C temperature point was omitted from the fit for reaction 1	4
4.	Schematic of DCA apparatus used to track droplet volume and contact angle as a function of time	9
5.	Schematic of processes occurring during evaporation and degradation of VX on a temperature-controlled impermeable substrate.	11
6.	Evolution of (a) droplet volume and (b) contact angle for an initial ~2 µL droplet of high-purity VX on a borosilicate glass substrate at temperatures of 20 °C (blue line), 40 °C (green line), and 60 °C (red line).....	15
7.	Evolution of (a) droplet volume and (b) contact angle for the initial ~2 µL droplets of EMPA (blue line), VX-pyro (green line), and VX-disulfide (red line) on a borosilicate glass substrate at a temperature of 60 °C.....	17
8.	Evolution of (a) droplet volume and (b) contact angle for an initial ~2 µL droplet of CASARM VX on a borosilicate glass substrate at temperatures of 40 °C (green line) and 60 °C (red line).....	18
9.	Evolution of (a) droplet volume and (b) contact angle for the initial ~2 µL droplets of a 90/10 v/v VX/EMPA mixture (solid lines) and a 95/5 v/v VX/EMPA mixture (dashed lines) on a borosilicate glass substrate at temperatures of 40 °C (green line) and 60 °C (red line).....	20
10.	Mixture of EMPA and VX-disulfide vigorously mixed in a vial and allowed to settle	22
11.	Relative amounts of VX and VX-disulfide remaining after 24 h vial reactor experiments at 60 °C, in various atmospheric conditions, with the amounts in the initial droplet (dose-confirmation sample) as the reference	24
12.	Fit of COMSOL evaporation models (solid lines) of EMPA (blue line), VX-pyro (green line), and VX-disulfide (red line) to experimental DCA data at 60 °C (open circles) by adjusting corresponding vapor pressures in the model.....	28

13. Simulated evolution of droplet volume for an initially 2 μL droplet containing 85% VX and 15% EMPA by moles at 60 $^{\circ}\text{C}$ (blue line) for different values of rate constant, $k_4 = 100 \text{ mol}^{-1} \text{ s}^{-1}$ (solid blue line), $500 \text{ mol}^{-1} \text{ s}^{-1}$ (dashed blue line), $1000 \text{ mol}^{-1} \text{ s}^{-1}$ (dash-dot blue line), and $5000 \text{ mol}^{-1} \text{ s}^{-1}$ (dotted blue line), and for comparison to corresponding experimental result (red line)29
14. Simulated evolution of composition in an initial 2 μL droplet containing 85% VX and 15% EMPA by moles at 60 $^{\circ}\text{C}$. (a) $k_4 = 100 \text{ mol}^{-1} \text{ s}^{-1}$, (b) $k_4 = 500 \text{ mol}^{-1} \text{ s}^{-1}$, (c) $k_4 = 1000 \text{ mol}^{-1} \text{ s}^{-1}$, and (d) $k_4 = 5000 \text{ mol}^{-1} \text{ s}^{-1}$ 30

TABLES

1.	Rate Constants for VX Degradation on Dry Sand Computed by Nuclear Magnetic Resonance (NMR) Experiments of Brevett et al.	4
2.	Summary of Physical Properties for VX and Degradation Byproducts	6
3.	High-Purity VX Mass in 2 μ L Droplets for Dose-Confirmation Samples and the Corresponding Fraction of the Expected Mass Delivered	7
4.	CASARM VX Mass in 2 μ L Droplets for Dose-Confirmation Samples and the Corresponding Fraction of the Expected Mass Delivered	7
5.	CASARM VX and EMPA Mass in 2 μ L Droplets for Dose-Confirmation Samples of 90/10 and 95/5 v/v VX/EMPA Mixtures and the Corresponding Mass and Mole Fractions of VX in Each Mixture	8
6.	Deposited High-Purity VX Droplet Volume and Mass and Corresponding Mass Remaining after DCA Experiments Performed at 20 and 60 °C.....	16
7.	Deposited CASARM VX Droplet Volume and Mass and Corresponding Masses of VX and EMPA Remaining after DCA Experiments (20 h after Contamination) Performed at 40 and 60 °C.....	18
8.	Deposited Droplet Volume and VX Mass and Corresponding Masses of VX and EMPA Remaining after DCA Experiments Performed at 40 and 60 °C Using 95/5 and 90/10 v/v VX/EMPA Mixtures	20
9.	Contact Angle Summary for VX and Related Byproducts at 60 °C.....	21
10.	Molar Amounts of VX, EMPA, and EA 2192 Remaining from an Initial Nominal 2 μ L Droplet of CASARM VX in a Sealed Vial at 60 °C for 24 h under Various Headspace Conditions.....	22
11.	Diffusivities of VX and Degradation Byproducts in Air at 60 °C as Computed by the Wilke–Lee Correlation	26

EVAPORATION AND DEGRADATION OF A SESSILE DROPLET OF VX ON AN IMPERMEABLE SURFACE

1. INTRODUCTION

In an explosive dissemination of a chemical warfare agent (CWA), a cloud of agent droplets with diameters on the order of 10–1000 μm can result,¹ which can subsequently be deposited on objects in the vicinity. Once the droplets are deposited on the surfaces of materials, they can spread, evaporate, and potentially absorb into the underlying material. Quantifying the rates of these processes is critical for predicting (1) how the agent is distributed and (2) the hazards that can result for personnel who may interact with these contaminated materials. These data are then used to implement the correct physical mechanisms in models that describe the absorption of agent in materials, such as the Decontamination System Performance Model (Decon SPM). The contamination process must be accurately modeled in the Decon SPM as all subsequent models and processes are based on an accurate description of the chemical composition and distribution of agent in and on the material.

This work stems from experimental efforts to quantify the evaporation rate of a sessile droplet of the CWA 2-(diisopropylamino)ethyl-*O*-ethyl methylphosphonothioate (VX) on impermeable borosilicate glass substrates using time-resolved imaging at temperatures ranging from 20 to 80 °C. At elevated temperatures (40 °C and higher), an unexpected behavior in the evaporation rate was observed (Figure 1). By monitoring the volume and contact angle of the droplet, two regimes of evaporation were identified, (1) a slow initial evaporation process, followed by (2) a nearly nonvolatile regime in which the evaporation rate dropped to near zero. The transition between evaporation rate regimes was accompanied by an increase in the contact angle of the droplet on the substrate. To enable accurate variable temperature modeling of contamination and decontamination processes, these transport and reaction processes must be understood at a mechanistic level.

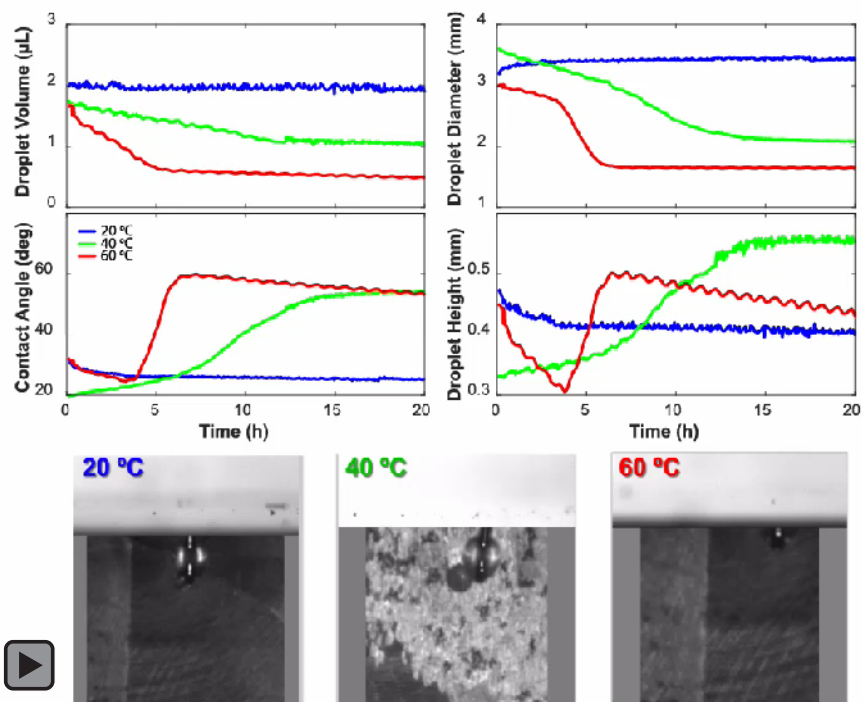


Figure 1. Video clip showing VX droplet evolution from 20 to 60 °C.

The transition between two distinct evaporation rate and contact angle regimes is indicative of a chemical change within the droplet during the evaporation process. It is known that VX degrades by an autocatalytic hydrolysis mechanism that was previously reported by Yang et al.² Based on auxiliary chemical analysis performed in this work (Fourier transform infrared [FTIR] spectroscopy, vial reactor), it is believed that the sessile droplet of VX degraded via the autocatalytic hydrolysis mechanism. The observed evaporation rate in the nearly nonvolatile regime agrees well with that of the degradation byproduct VX-disulfide, whereas the observed contact angle in this regime agrees well with those of the degradation byproducts ethylmethylphosphonic acid (EMPA) and VX-pyro. The chemical analysis shows that these byproducts coexist in the droplet, which suggests that spinodal decomposition (i.e., phase separation) occurs during the degradation process and separates the droplet into a hydrophilic core consisting of EMPA and VX-pyro and a hydrophobic shell consisting of VX-disulfide. Additional experiments were performed by mixing equal parts of EMPA and VX-disulfide in a vial, thereby confirming that these two species are immiscible. However, additional experimentation is needed to definitively prove that phase separation occurs. To accompany the experimental work, continuum models of the combined evaporation and degradation processes were developed, and simulations were able to reproduce the correct change in composition with time. But it appears that phase separation must be included to predict the experimentally observed evaporation rate.

Literature Review for the VX Degradation Mechanism

The autocatalytic hydrolysis mechanism for the degradation of VX was previously described by Yang et al.² By obtaining kinetic data for VX degradation on both wet and dry sand, this mechanism was expanded upon by Brevett et al.³ A schematic of the autocatalytic hydrolysis mechanism is depicted in Figure 2.

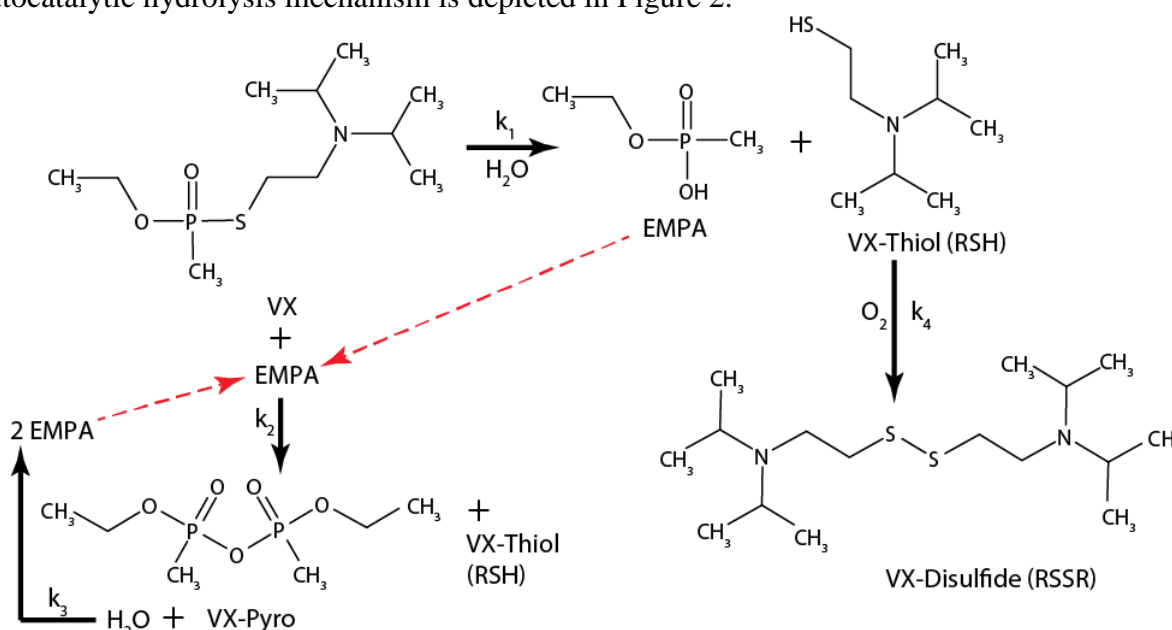


Figure 2. Schematic of autocatalytic hydrolysis of VX, reproduced from Brevett et al.³ Solid black lines indicate reaction pathways, and dashed red lines indicate how EMPA, produced during the reaction process, acts as an autocatalytic species.

As shown in reaction 1 (Figure 2), when moisture is present, VX will react to form EMPA and a thiol, VX-thiol (RSH). Over time, the VX will react with the byproduct of reaction 1 (EMPA) and generate VX-pyro (Pyro in reaction 2). In reaction 3, the byproduct of reaction 2 (Pyro) reacts with the available water and degrades into two EMPA molecules. Finally, in reaction 4, the VX-thiol reacts with oxygen in the atmosphere to produce VX-disulfide (RSSR). The dashed red arrows in Figure 2 indicate that EMPA formed via reactions 1 and 3 can serve as a reactant feed for reaction 2, which results in an autocatalytic mechanism. The mechanism of Figure 2 is shown in equation form below. From the autocatalytic degradation mechanism, it is clear that water or EMPA is needed to jump-start the degradation process. Another common byproduct of VX is EA 2192, but as shown in the results, it was not present in significant quantities in any of the experiments performed in this work.





Brevett et al.³ also provided values for the rate constants (k) for reactions 1–3 (Table 1), but did not explicitly include the amount of water or oxygen in computing these rate constants. The rates are expressed in terms of number of moles of each species (n_i). The kinetic data obtained by Brevett et al. was fit to an Arrhenius law as shown in Figure 3. The variable experimental temperatures are compared to this reaction network and rate constants later in this report.

Table 1. Rate Constants for VX Degradation on Dry Sand Computed by Nuclear Magnetic Resonance (NMR) Experiments of Brevett et al.³

Reaction	Rate Expression	Units	Rate Constants, k_i			
			22 °C	30 °C	40 °C	50 °C
r_1	$r_1 = k_1 n_{\text{VX}}$	h^{-1}	0.00013	0.014	0.031	0.055
r_2	$r_2 = k_2 n_{\text{VX}} n_{\text{EMPA}}$	$\text{mol}^{-1} \text{h}^{-1}$	2618	4474	9627	12222
r_3	$r_3 = k_3 n_{\text{Pyro}}$	h^{-1}	0.75	0.146	0.067	0.026

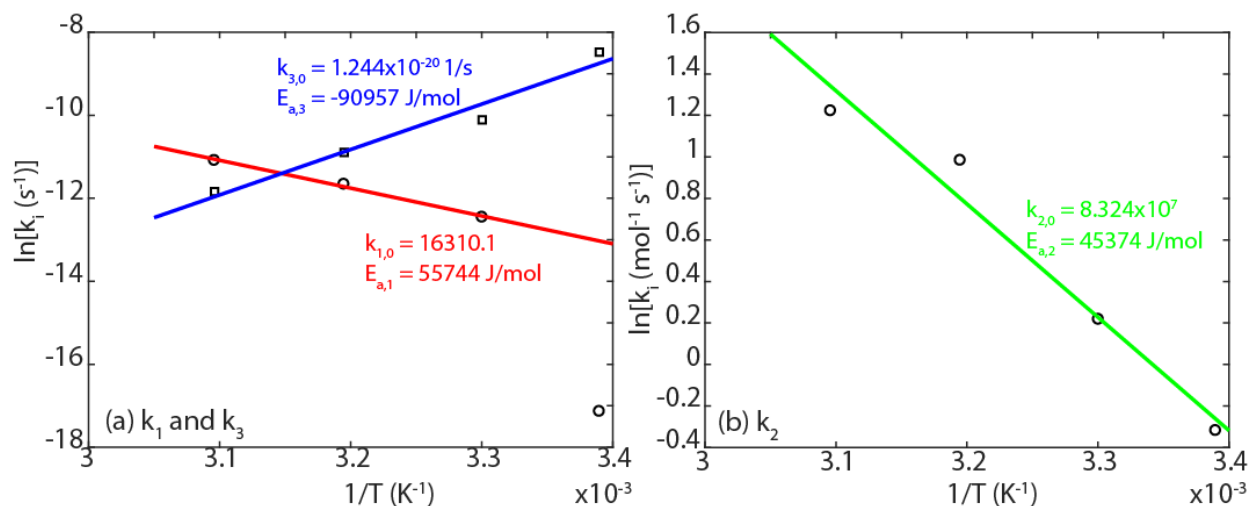


Figure 3. Fit of kinetic data determined by Brevett et al. to an Arrhenius law. The 22 °C temperature point was omitted from the fit for reaction 1.

2. METHODS AND MATERIALS

The primary goal of this work was to study the relationship between the observed evaporation rate and contact angle of a sessile droplet of VX and to determine the corresponding change in composition as a result of the degradation byproducts. For this reason, it is important to know the critical properties of VX and its degradation byproducts (Section 2.1).

Chromatography using liquid chromatography (LC)/tandem mass spectroscopy (MS/MS) and gas chromatography (GC)/mass spectroscopy (MS) were the primary methods used to quantify the composition of the sessile droplet (Section 2.2).

Time-resolved values of droplet diameter, height, and contact angle were obtained with top-down and side-on image analysis. These values were then used to fit a spherical cap model and determine the droplet volume as a function of time to provide evaporation rate (Section 2.3).

After some of the dynamic contact angle (DCA) experiments, the remaining droplet was transferred to the surface of a diamond attenuated total reflection (ATR) crystal, and the infrared spectrum of the droplet was obtained to provide further qualitative information on the chemical composition of the final state of the droplet (Section 2.4).

In addition, observations were made to determine the effect of varying amounts of water vapor and oxygen on the final chemical composition of the droplet. To accomplish this, vial reactor experiments were carried out by aging droplets of VX for 24 h at 60 °C in sealed glass vials that were filled with gas mixtures of varying oxygen and humidity content. Afterward, chemical analysis of the final droplet (Section 2.2) was used to help decipher how the resulting product composition depended on the oxygen and humidity content of the surroundings (Section 2.6).

Mathematical models for the evaporation and degradation processes of the sessile VX droplet were also developed and solved using the commercially available, finite-element solver software COMSOL (COMSOL, Inc.; Burlington, MA). This allowed comparison of the experimentally observed evaporation rates and chemical compositions to those predicted under certain assumptions (Section 2.7).

2.1 Chemicals

The agent chemicals used in this study were both high-purity (89.0%) and Chemical Agent Standard Analytical Reference Material (CASARM) (>98% purity) grades of VX. (Note: Despite the designation, high-purity VX is only 89% pure, whereas CASARM-grade VX is over 98% pure.) It is important to keep this in mind for proper interpretation of the results. Purity information was obtained from either NMR, GC/MS, or LC/MS analyses (Section 2.2). Lot information and chemical analysis for the high-purity and CASARM-grade VX are given in the agent purity certificates in the appendix. The chemical agents were used only in properly certified surety facilities that were capable of handling such chemicals safely, and the personnel handling the chemical agents for this study were fully trained and certified for such operations.

Some of the experiments used the following VX degradation byproducts:

- EMPA from Sigma-Aldrich (St. Louis, MO) 386561-1G, lot no. 16327DD, 98% purity;
- VX-disulfide produced in-house from U.S. Army Edgewood Chemical Biological Center (ECBC; Aberdeen Proving Ground, MD);
- VX-pyro produced in-house from ECBC; and
- VX-thiol produced in-house from ECBC, NB-04-0057-51, 99% purity.

The relevant physical properties molecular weight, density, log octanol–water partition coefficient ($\text{Log } K_{o/w}$), and vapor pressure of VX and its byproducts are provided in Table 2; vapor pressure values were derived and are described in Section 4.2 herein.

Table 2. Summary of Physical Properties for VX and Degradation Byproducts

Chemical	Molecular Weight (g/mol)	Density at 20 °C (g/mL)	$\text{Log } K_{o/w}$ ⁴	Vapor Pressure at 60 °C (Pa)
VX	267	1.004	2.06	3.2
EMPA	124	1.17	−0.15	7.25
VX-pyro	230	1.18	−0.5	4
VX-thiol	161	0.883	2.29	444
VX-disulfide	321	0.952	4.9	0.35
Water	18	1	−∞	19771

2.2 Chromatographic Chemical Analysis

Samples were analyzed by LC/MS/MS (Agilent 1200/1290 series LC system and Applied Biosystems [Life Technologies Corporation, Carlsbad, CA] API5000/5500 triple-quadrupole mass spectrometer equipped with a TurboV ion source) after dilution and the addition of an internal standard to quantify the mass of VX and its primary phosphorus-containing reaction byproducts, EMPA and ethyl methylphosphonothioic acid (EA 2192). LC was performed using a mobile phase that consisted of 5 mM ammonium acetate and 0.1% formic acid. Mobile phase A (MPA) was 95% water/5% 2-propanol and mobile phase B (MPB) was 5% water/95% 2-propanol. Chromatography was performed using an isocratic flow configuration (50% MPA/50% MPB) with an Agilent Technologies Zorbax SB-C18, Rapid Resolution 4.6×75 mm, $3.5 \mu\text{m}$ particle size column (part no. 866953-902). VX was analyzed using the electrospray ionization, multiple-reaction method (MRM) ion transition of 268.1–128.0. EMPA was analyzed using MRM transitions of 123.0–94.8, and EA 2192 analysis involved MRM transitions of 240.1–128.0.

Samples were analyzed by GC/MS (Agilent 6890 GC and an Agilent 5975C inert XL mass selective detector with triple-axis detector) after dilution to detect the presence of the VX reaction byproduct, VX-disulfide. The chromatography was performed using a 30 m \times 0.250 mm \times 0.25 μ m HP-5ms UI capillary column (part no. 19091S-433UI), with helium as the carrier gas. VX-disulfide was analyzed by electron ionization MS in SIM/scan mode using ion fragments with mass-to-charge ratios of 72, 114, 144, 160, and 193.

2.2.1 High-Purity VX Dose-Confirmation Samples

Before performing two of the DCA tests (Section 3.1), chemical analysis (Section 2.2) was performed on a 2 μ L droplet of high-purity VX. Five droplets were analyzed in this manner for each of the two DCA experiments. Based on the density of VX (1.004 g/mL),⁵ the mass of VX expected to be delivered was 2.008 mg. Table 3 shows the mass actually delivered, which was determined on the basis of chemical analysis, along with the expected value. From this analysis, the VX purity was between 81 and 89% by mass of that of the CASARM VX for these experiments.

Table 3. High-Purity VX Mass in 2 μ L Droplets for Dose-Confirmation Samples and the Corresponding Fraction of the Expected Mass Delivered

Experiment	VX Mass Delivered (mg)	Expected VX Mass Delivered (mg)	Fraction of Expected VX Mass Delivered
20 °C, Replicate 1	1.7827 \pm 0.0587	2.008	0.89
60 °C, Replicate 1	1.6248 \pm 0.0822	2.008	0.81

2.2.2 CASARM VX Dose-Confirmation Samples

Before the DCA tests were performed with CASARM VX (Section 3.3), a 2 μ L droplet of CASARM VX was deposited into 20 mL of isopropyl alcohol (IPA), and chemical analysis was performed to determine the mass of VX in the droplet. Five droplets were analyzed in this manner for each of the two DCA experiments (one at 40 °C and the other at 60 °C). Based on the density of VX (1.004 g/mL),⁵ the expected delivered mass of VX was 2.008 mg. Table 4 shows the actual delivered mass, based on the chemical analysis, along with the expected value. From this analysis, the quantity of CASARM VX delivered was as expected.

Table 4. CASARM VX Mass in 2 μ L Droplets for Dose-Confirmation Samples and the Corresponding Fraction of the Expected Mass Delivered

Experiment	VX Mass Delivered (mg)	Expected VX Mass Delivered (mg)	Fraction of Expected VX Mass Delivered
40 °C	1.960 \pm 0.037	2.008	0.98
60 °C	2.073 \pm 0.075	2.008	1.03

2.2.3 CASARM VX/EMPA Mixtures Dose-Confirmation Samples

Two mixtures of VX and EMPA were created: (1) a 90/10 v/v VX/EMPA mixture and (2) a 95/5 v/v VX/EMPA mixture. The VX used to create these mixtures was the CASARM VX (>98% purity), which is described in Section 2.2.2. Before the DCA tests with the VX/EMPA mixtures were performed, a 2 μ L droplet of the mixture was deposited into 20 mL of IPA, and chemical analysis was performed to determine the mass of VX in the droplet. Five droplets were analyzed in this manner for each of the two mixture compositions. Table 5 shows the resulting compositions (by mass and mole) for these mixtures. These results demonstrate that the mixture compositions were close to the intended values.

Table 5. CASARM VX and EMPA Mass in 2 μ L Droplets for Dose-Confirmation Samples of 90/10 and 95/5 v/v VX/EMPA Mixtures and the Corresponding Mass and Mole Fractions of VX in Each Mixture

VX/EMPA (v/v)	VX Mass Delivered (mg)	EMPA Mass Delivered (mg)	Fraction VX by Mass	Fraction VX by Mole
90/10	1.921 ± 0.117	0.169 ± 0.031	0.916 ± 0.0004	0.840 ± 0.127
95/5	1.915 ± 0.046	0.107 ± 0.0028	0.945 ± 0.001	0.891 ± 0.002

2.3 DCA Experiments

Detailed descriptions of the apparatus and procedures used to perform the DCA experiments are described elsewhere.⁶ The contact angle analyzer apparatus (First Ten Ångströms 1000C; Portsmouth, VA) enabled simultaneous top-down and profile viewing of the droplet evolution via two independent cameras (both Prosilica GC750; Allied Vision; Exton, PA). Temperature control of the glass substrate, which served as the substrate for the deposited VX droplets, was achieved via a Peltier element. The substrate was enclosed in an aluminum housing with glass windows to shield the droplet from the strong airflow in the fume hood. The liquid droplet (1 or 2 μ L) was delivered to the substrate via a 10 μ L syringe (Hamilton Gastight syringe, model 1701 N SYR; Hamilton Company; Reno, NV) that was mounted on a three-axis actuator. A schematic of the DCA apparatus is shown in Figure 4.

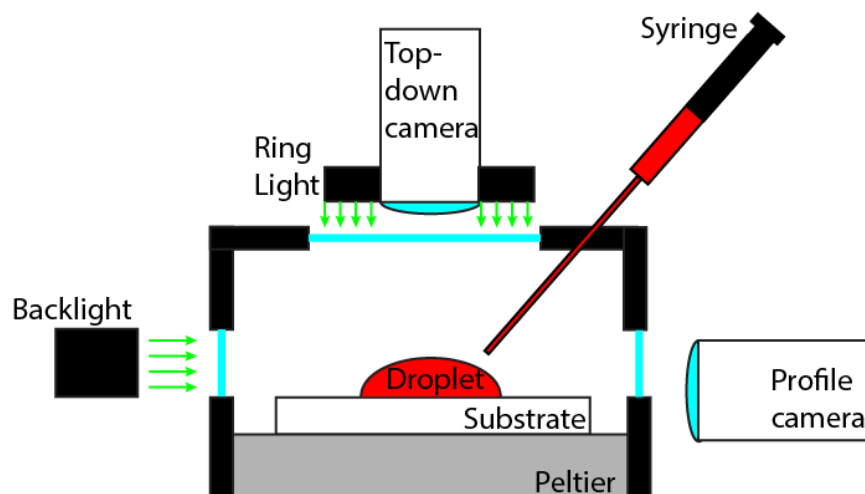


Figure 4. Schematic of DCA apparatus used to track droplet volume and contact angle as a function of time.

Image acquisition was controlled at a rate of 0.5 Hz by the software. The acquired images were analyzed to obtain the droplet radius, height, and contact angle as a function of time. The droplet volume was computed from the measured parameters under the assumption that the droplet had the shape of a spherical cap. Measurements were typically taken for 24 h, unless otherwise noted. In some of the tests, the remaining liquid on the glass substrate was subject to chemical analysis (Section 2.2).

2.4 Phase-Separation Experiments

Equal parts (~1 mL) of EMPA and VX-disulfide were put into a GC vial and vigorously mixed. The mixture was allowed to settle, and the vial was photographed to determine if the two components were miscible.

2.5 Infrared Spectroscopy Experiments

After some of the DCA experiments, the residual liquid on the glass substrate was transferred to a single-bounce ATR accessory (Specac Golden Gate, diamond ATR crystal; Fort Washington, PA) and analyzed on a Thermo-Nicolet 670 FTIR spectrometer (Thermo Scientific; Sunnyvale, CA). Scans were taken from 4000 to 650 cm^{-1} with a resolution of 2 cm^{-1} , which yielded the IR absorbance spectrum of the residual liquid from the DCA experiment. Similar scans were also performed for neat liquids to provide reference spectra that would aid in interpretation of the spectra for the liquid mixtures.

2.6 Vial Reactor Experiments

Vial reactor experiments were run for the following gas conditions: (1) ambient air, (2) dry air (estimated $-40\text{ }^{\circ}\text{C}$ dew point), (3) humidified air, (4) dry argon, and (5) humidified argon. Vial reactors consisted of 10 mL glass vials with penetrable silicon/polytetrafluoroethylene septum caps. The vials for the argon and the dry air conditions were placed in a drying oven at an elevated temperature overnight and then cooled in a desiccator.

When they were cool, vials, caps, and septa were transferred to a glove bag, purged with the appropriate gas, and capped before they were removed from the glove bag. The humidified conditions were achieved by placing a narrow, open glass vial insert containing 5 μL of deionized water into the reactor vial, filling the vial with gas, and capping it. The ambient air vials were simply capped in the laboratory air environment with no other special preparations. The reactors were injected through the septum with a 2 μL droplet of VX and placed in a 60 $^{\circ}\text{C}$ culture tube incubator for 24 h. After the reaction period, the entire contents of the reactor were diluted in 5 mL of IPA, mixed well, and then diluted further for analysis. Chemical analysis (Section 2.2) was performed to determine the quantity of VX and its byproducts that remained at the end of the experiment.

2.7 Mathematical Models and Simulations

A mathematical model of the combined evaporation and degradation process was formulated under the assumptions that (1) the contact angle of the liquid droplet did not change during the evaporation process, (2) the droplet remained well-mixed throughout the process, (3) the liquid behaved as an ideal solution, and (4) the kinetics described by Brevett et al. applied.³

The following comments apply to the aforementioned assumptions:

1. Although a change in contact angle can be observed experimentally, a correct simulation of this change would require knowledge of the contact angle as a function of chemical composition within the droplet. This information is not currently readily available.
2. An upper limit on the time scale of mixing can be approximated by assuming that there are no convective currents in the droplet (i.e., diffusion is the only transport mechanism in the droplet). In this test, the mixing time scale was given by L^2/D , where L is the length scale of the droplet and D is the diffusivity of chemical species in the droplet. For the experiments performed in this work, L was ~ 1 mm and D was $\sim 10^{-9}$ m^2/s , and the time scale of mixing was approximately 0.5 h. As will be shown later, the reaction occurred on the order of 5 h at 60 $^{\circ}\text{C}$.
3. It is unlikely that the liquid mixture behaves as an ideal solution throughout the evaporation and degradation process. However, in the absence of reliable vapor–liquid equilibrium (VLE) data for mixtures of VX and its byproducts as a function of composition, the first-order approximation of an ideal solution was made to facilitate calculations.
4. The kinetics reported by Brevett et al. do not explicitly account for the molar amount of water (i.e., the molar amount of water is embedded in the corresponding rate constants). By assuming that these rate constants are applicable, it is also assumed that the same relative amount of water is in the system throughout the entire evaporation and degradation process.

A schematic of the processes is shown in Figure 5.

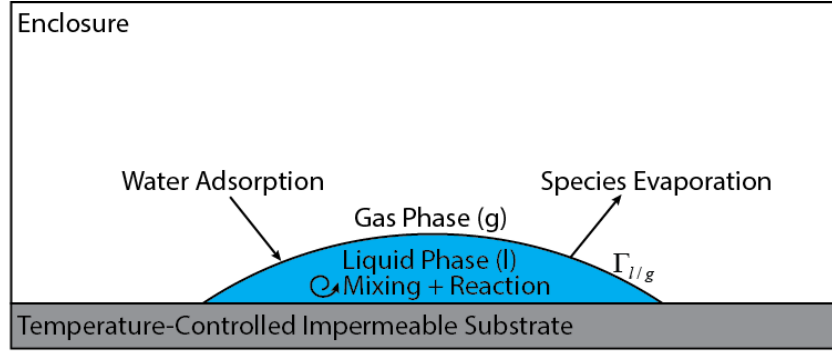


Figure 5. Schematic of processes occurring during evaporation and degradation of VX on a temperature-controlled impermeable substrate.

In the liquid phase, the following species balance equations (eqs 5–9) apply based on the VX degradation mechanism presented in eqs 1–4.

$$\frac{dn_{\text{VX},l}}{dt} = -k_1 n_{\text{VX},l} - k_2 n_{\text{VX},l} n_{\text{EMPA},l} - \int_{A_d} n''_{\text{ev,VX}} dA \quad (5)$$

$$\frac{dn_{\text{EMPA},l}}{dt} = k_1 n_{\text{VX},l} - k_2 n_{\text{VX},l} n_{\text{EMPA},l} + k_3 n_{\text{Pyro},l} - \int_{A_d} n''_{\text{ev,EMPA}} dA \quad (6)$$

$$\frac{dn_{\text{Pyro},l}}{dt} = k_2 n_{\text{VX},l} n_{\text{EMPA},l} - k_3 n_{\text{Pyro},l} - \int_{A_d} n''_{\text{ev,Pyro}} dA \quad (7)$$

$$\frac{dn_{\text{RSH},l}}{dt} = k_1 n_{\text{VX},l} + k_2 n_{\text{VX},l} n_{\text{EMPA},l} - k_4 n_{\text{RSH},l}^2 - \int_{A_d} n''_{\text{ev,RSH}} dA \quad (8)$$

$$\frac{dn_{\text{RSSR},l}}{dt} = k_4 n_{\text{RSH},l}^2 - \int_{A_d} n''_{\text{ev,RSSR}} dA \quad (9)$$

where

$n_{i,l}$ is moles of species i in the liquid phase l (mol m^{-3});

k_i is rate constant for reaction in the VX degradation mechanism (variable units);

- $n''_{ev,i}$ is evaporation flux of species i from the droplet (mol/m²);
- V_d is droplet volume (m³); and
- A_d is interfacial area between liquid droplet and surrounding gas phase (m²).

Species transport equations must also be solved in the gas phase, g , and spatial gradients are accounted for in the gas phase due to the relatively large size of the enclosure compared to the droplet.

$$\frac{\partial C_{i,g}}{\partial t} = \nabla \cdot (D_{i,g} \nabla C_{i,g}) + \frac{1}{V_d} \int_{A_d} n''_{ev,i} dA \quad (10)$$

where

- $C_{i,g}$ is concentration of species i in the gas phase (mol m⁻³); and
- $D_{i,g}$ is diffusivity of species i in the gas phase (m² s⁻¹).

These equations are subject to mass conservation and thermodynamic equilibrium at the gas–liquid interface (subject to the aforementioned assumption 3, that the liquid behaves as an ideal solution).

$$n''_{ev,i} = D_{i,g} \nabla C_{i,g} \cdot \mathbf{n}_{lg} \quad (11)$$

$$C_{i,g}(\Gamma_{g/l}) = \frac{p_{i,vap}}{RT} x_{i,l} \quad (12)$$

where $x_{i,l}$ is the mole fraction of species i (j for the summation) in the liquid l given by

$$x_{i,l} = \frac{n_{i,l}}{\sum_j n_{j,l}} \quad (13)$$

The droplet volume is tracked using the following auxiliary equation:

$$V_d = \frac{\sum_j MW_j n_{j,l}}{\rho_l} \quad (14)$$

where MW is molecular weight.

These equations were implemented in the COMSOL software (v. 5.1)⁷ using the ordinary differential equation (ODE) solver for the liquid-phase equations (eqs 5–9) and the Transport of Dilute Species module for the gas-phase equations (eq 10) and their corresponding boundary conditions (eq 12).

3. RESULTS

The experimental results are presented in chronological order primarily to illustrate the evolution in thinking about the problem as the investigation proceeded. For this reason, a brief overview is presented before the details of each experiment are given to provide the reader with perspective on the overarching goals of this work.

This experimental investigation began by attempting to determine the evaporation rate of high-purity VX (~89% pure) at temperatures from 20 to 60 °C (Section 3.1) to verify the transport models used to describe droplet evaporation. This was done by performing DCA experiments to determine the time evolution of droplet volume and contact angle. During data analysis, it was found that at temperatures of 40 °C and above, the droplet evaporation rate unexpectedly displayed two distinct regimes: (1) a semivolatile regime followed by (2) a nearly nonvolatile regime. At the abrupt transition between these two regimes, the contact angle increased from ~30 to ~60°. The abrupt change in evaporation rate and contact angle suggested that a chemical change occurred within the droplet, which was confirmed via chemical analysis (Section 2.2).

Reading of the literature led to the suggestion that the chemical change within the droplet was likely due to a known autocatalytic hydrolysis mechanism for VX degradation. For this reason, DCA experiments were carried out independently on each of the known byproducts of the degradation at 60 °C, namely EMPA, VX-pyro, and VX-disulfide (Section 3.2). It was determined that the evaporation rate of each chemical was constant and that the constant rate of VX-disulfide evaporation was approximately equal to the evaporation rate of high-purity VX as observed in the second regime. Furthermore, the initial contact angle of EMPA and VX-pyro roughly corresponded to the contact angle of high-purity VX at the start of the second regime.

One potential issue with the DCA experiments on high-purity VX (~89% pure) was that the influence of the remaining ~11% on the results was not well known. To explore this further, DCA experiments were performed for CASARM VX (>98% pure) (Section 3.3). It was found that the evaporation rate displayed an additional slower evaporation rate at the start of the process compared with high-purity VX, which was because of the initial lack of EMPA in the

droplet to promote the degradation process. This provided additional evidence that the autocatalytic degradation mechanism was driving the observed process.

The influence of the initial amount of EMPA in the VX droplet was investigated further by creating known mixtures of EMPA and CASARM VX and performing DCA experiments (Section 3.4). It was found that the higher quantity of EMPA resulted in a higher evaporation rate in the initial regime and an earlier transition to the nearly nonvolatile regime. The additional EMPA appeared to increase the overall rate of the autocatalytic degradation process.

All DCA experiments to this point were performed under atmospheric conditions at controlled temperatures (i.e., air with atmospheric humidity). Another set of experiments was performed on 2 μL droplets of high-purity VX in sealed vial reactors that were purged with varying amounts of oxygen and humidity to determine the influence of these factors on the final droplet composition (Section 2.2.1). In this case, it was found that oxygen does not play a key role in the conversion of VX, but humidity does influence the results. The more-humid conditions drive the conversion of VX to near completion, whereas drier conditions result in a lesser conversion of VX. Chemical analysis (Section 2.2) revealed that the primary byproducts of VX were EMPA and VX-disulfide, and that it was likely that VX-pyro persisted as a byproduct under drier conditions due to the lack of available water to convert VX to EMPA.

3.1 DCA Results for High-Purity VX

A 2 μL droplet of high-purity VX (Section 2.2.1) was deposited on a borosilicate glass substrate and allowed to age at 20, 40, and 60 $^{\circ}\text{C}$ for a 20 h period. The resulting changes to the high-purity VX droplet volume during this test are shown in Figure 6a. For the 20 $^{\circ}\text{C}$ test, the droplet volume decreased by less than 5% over the observation time (t). For the 40 and 60 $^{\circ}\text{C}$ tests, the droplet volume displayed two clearly distinct regimes of evaporation rate (denoted by the dotted black lines in Figure 6a) and showed a relatively sharp transition between them. This suggested that the chemical composition in the droplet was changing. For the 40 $^{\circ}\text{C}$ test, the first regime between the deposition of the droplet and 10 h later, the evaporation rate was $\sim 0.06 \mu\text{L/h}$, and in the second regime after 11 h, the evaporation rate was $\sim 0.006 \mu\text{L/h}$. For the 60 $^{\circ}\text{C}$ test, the evaporation rate was $\sim 0.25 \mu\text{L/h}$ in the initial regime ($t < 4 \text{ h}$), and the second regime ($t > 5 \text{ h}$) displayed an evaporation rate of $0.009 \mu\text{L/h}$.

The contact angle experiments also displayed two distinct regimes, and the time at which the transition occurred roughly corresponded to the transition between evaporation rate regimes. The same droplet, which had an initial contact angle between 20 and 30 $^{\circ}$, showed an increase to a contact angle between 50 and 60 $^{\circ}$ after the transition between evaporation rates. The rate at which the contact angle changed was larger for the 60 $^{\circ}\text{C}$ test as compared with the 40 $^{\circ}\text{C}$ test.

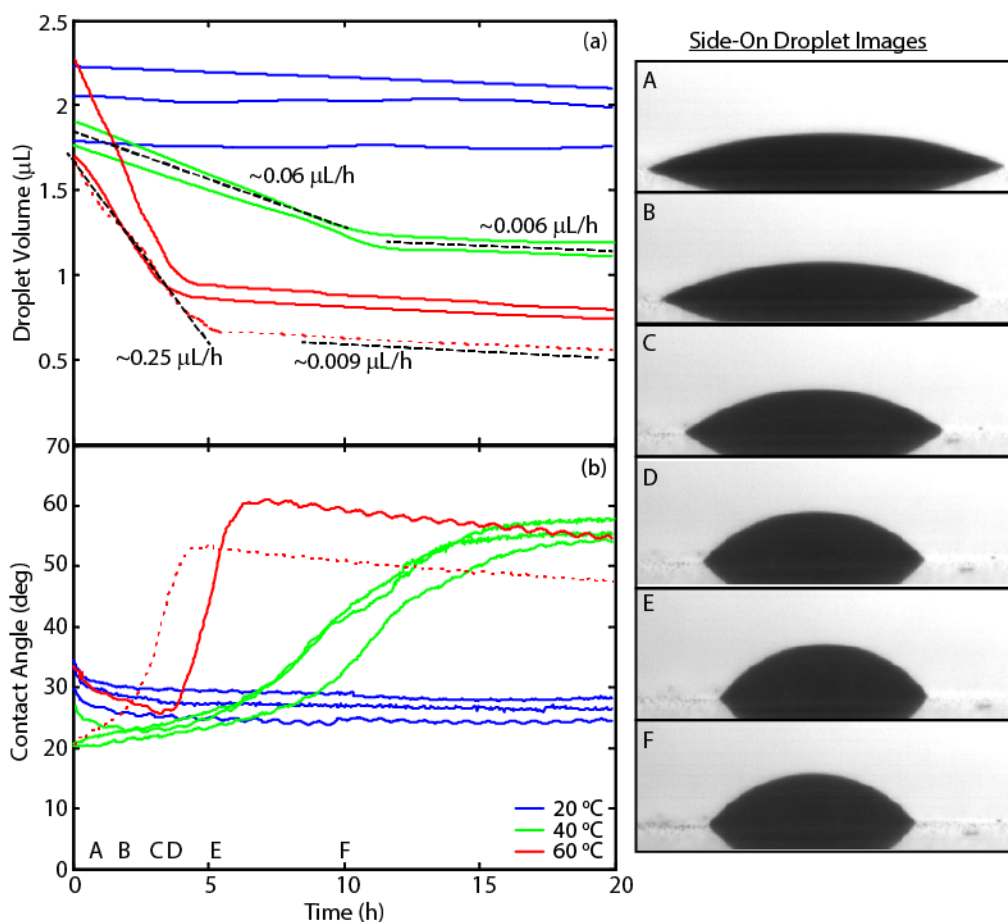


Figure 6. Evolution of (a) droplet volume and (b) contact angle for an initial $\sim 2 \mu\text{L}$ droplet of high-purity VX on a borosilicate glass substrate at temperatures of 20 °C (blue line), 40 °C (green line), and 60 °C (red line). Dotted black lines and corresponding annotations indicate the approximate droplet evaporation rates. Shown on the right are side-on images of the droplet that correspond to the dotted lines on the droplet volume and contact angle plots at the indicated times (A–F) for the 60 °C test.

The division of evaporation rate and contact angle into two distinct regimes with a sharp transition likely signified a change in the chemical composition of the VX droplet, which was possibly the autocatalytic hydrolysis of the VX, as discussed herein. Therefore, the fractional amount of VX remaining in the droplet for the 40 and 60 °C tests should have been significantly different from that in the 20 °C test, which displayed a constant evaporation rate. To demonstrate this, chemical analysis was employed to determine the amount of VX in the final droplets for both the 20 and 60 °C tests (Table 6). The results showed that for the 60 °C test, 2% VX by mass remained, which supported the conclusion that a chemical change occurred. Furthermore, the relative sharpness of the transition between regimes for the volume and contact angle measurements suggested that (1) the more-volatile byproducts evaporate eventually, leaving the less-volatile byproducts behind, or (2) the droplet undergoes phase separation at some (temperature-dependent) composition, and the more-volatile species is at the core of the droplet, whereas the less-volatile species is in the shell of the two-phase droplet.

Table 6. Deposited High-Purity VX Droplet Volume and Mass and Corresponding Mass Remaining after DCA Experiments Performed at 20 and 60 °C

Experiment	Initial Droplet Volume (μL)	VX Mass Delivered (mg)	VX Mass Remaining (mg)	Fraction of VX Mass Remaining
20 °C, Replicate 1	2.05	1.8272	1.4905	0.815
60 °C, Replicate 1	1.68	1.3648	0.0255	0.019

3.2 DCA Results for Degradation Byproducts

To help understand the evolution of droplet volume and contact angle observed for high-purity VX (Section 3.1), DCA experiments were carried out on liquid forms of the VX degradation byproducts EMPA, VX-pyro, and VX-disulfide at a temperature of 60 °C. The evolution of droplet volume and contact angle is shown for each of these compounds in Figure 7. The evaporation rates of EMPA and VX-pyro were constant and nearly identical ($\sim 0.05 \mu\text{L/h}$), whereas the constant evaporation rate of VX-disulfide was an order of magnitude less at ($\sim 0.008 \mu\text{L/h}$). The contact angles of EMPA and VX-pyro also behaved in a nearly identical manner, beginning at about 57° and decreasing to about 30° after 20 h. VX-disulfide had a much lower contact angle that started at $\sim 13^\circ$ and ended at $\sim 12^\circ$ after 20 h.

The evaporation rate for VX-disulfide of $\sim 0.008 \mu\text{L/h}$ at 60 °C was approximately equal to the evaporation rate of high-purity VX in the second regime of $0.009 \mu\text{L/h}$ at 60 °C (Figure 6a). This suggested that the evaporation rate of high-purity VX in the nearly nonvolatile second regime was controlled by the presence of VX-disulfide. However, there was a large discrepancy between the contact angle of VX-disulfide at 60 °C and that of high-purity VX in the second evaporation regime at 60 °C, which indicated that the remaining byproduct of the VX evaporation and degradation process was not solely VX-disulfide.

On the other hand, the initial contact angle of EMPA and VX-pyro ($\sim 57^\circ$) closely corresponded to the contact angle observed for high-purity VX after the transition to the second evaporation rate regime ($\sim 50\text{--}60^\circ$). This suggested the possibility that the transition between evaporation rate and contact angle regimes in high-purity VX was induced by a phase-separation process in which the core of the sessile droplet consisted of the degradation byproducts EMPA and VX-pyro (controlling the contact angle), whereas the shell consisted of VX-disulfide (controlling the evaporation rate). However, it is emphasized that the experimental observations do not conclusively indicate the described phase-separation process. Another possibility could be related to Marangoni flows, where nonuniform evaporation from the droplet generates heterogeneous distributions of the chemical species within the droplet, which influences contact angles and evaporation rates.^{8,9}

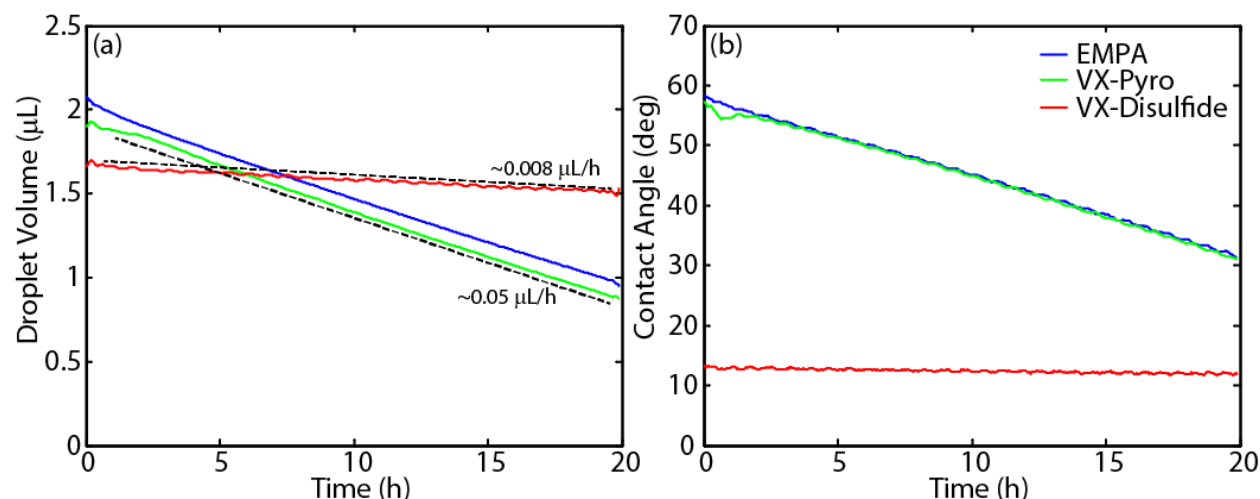


Figure 7. Evolution of (a) droplet volume and (b) contact angle for the initial ~ 2 μL droplets of EMPA (blue line), VX-pyro (green line), and VX-disulfide (red line) on a borosilicate glass substrate at a temperature of 60 °C. Dotted black lines and corresponding annotations indicate approximate droplet evaporation rates.

3.3 DCA Results for CASARM VX

The effects of impurities in the initial VX droplet were mostly eliminated by using CASARM VX. The evolution of an initially nominal 2 μL droplet of CASARM VX ($>98\%$ purity) on a borosilicate glass substrate over a 20 h period is shown in Figure 8a for temperatures of 40 and 60 °C. For the 40 °C test, the droplet displayed an initial long period (~ 13 h) of slow evaporation at a constant rate of about 0.012 $\mu\text{L/h}$, followed by a transition to a faster evaporation rate of ~ 0.07 $\mu\text{L/h}$ for the remainder of the experiment. This second regime of evaporation corresponded closely with that of the first regime for high-purity VX at 40 °C (~ 0.06 $\mu\text{L/h}$, Figure 6a). For the 60 °C test with CASARM VX, the initial evaporation rate was ~ 0.11 $\mu\text{L/h}$ for the first 4 h of the experiment, transitioned to ~ 0.28 $\mu\text{L/h}$ from ~ 4 to 6 h, and then finally settled into a slow evaporation rate regime of ~ 0.01 $\mu\text{L/h}$ for the remainder of the experiment. The second evaporation rate regime for CASARM VX at 60 °C corresponded closely with that of the initial regime for high-purity VX at 60 °C (~ 0.25 $\mu\text{L/h}$, Figure 6a). In addition, the final evaporation rate regime for the CASARM VX test at 60 °C closely corresponded with that of high-purity VX at 60 °C (~ 0.009 $\mu\text{L/h}$).

Based on these observations, it appears that for CASARM VX, there was an additional slow evaporation rate regime at the start of the process before it transitioned to what was observed in the initial regime for high-purity VX. The length of this additional initially slow evaporation regime was longer for the 40 °C test (~ 13 h) as compared with the 60 °C test (~ 4 h). One possible explanation is that the high-purity VX contained a sufficient amount of EMPA in the initial VX droplet, so that reactions 1 and 2 (eqs 1 and 2) of the degradation mechanism occurred. The EMPA and VX-pyro byproducts have relatively higher evaporation rates, which cause the droplet volume to decrease faster. However, in the case of CASARM VX, there was no EMPA in the initial droplet; therefore, only reaction 1 (eq 1) initially occurred with water vapor in the surrounding air until a sufficient amount of EMPA was generated, causing reaction 2 to

occur to an observable extent. In addition, the presence of EMPA in the high-purity VX could draw water vapor from the surrounding air into the droplet at a faster rate due to its hygroscopic nature. In the CASARM VX, the rate of water transfer from the surrounding air could be relatively slower, and if reaction 1 was rate-limited by the water transfer from the surrounding air, then the degradation rate would be correspondingly slower.

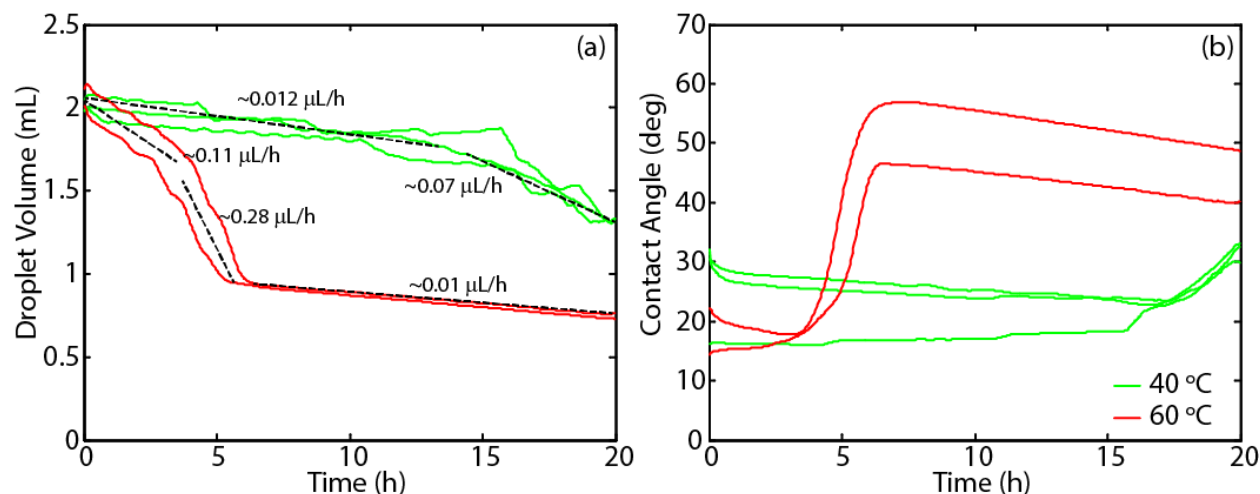


Figure 8. Evolution of (a) droplet volume and (b) contact angle for an initial $\sim 2 \mu\text{L}$ droplet of CASARM VX on a borosilicate glass substrate at temperatures of 40 °C (green line) and 60 °C (red line). Dotted black lines and corresponding annotations indicate approximate droplet evaporation rates at different time intervals during the experiment.

To determine the amounts of VX, EMPA, and EA 2192 remaining in the droplets after the 40 and 60 °C DCA experiments, chemical analysis was performed. The initial deposited droplet volume and VX mass for each of these experiments are shown in Table 7 along with the VX and EMPA mass remaining after the DCA experiment. It was determined that the mass of EA 2192 was less than 1% of the mass of VX and EMPA in the mixture.

Table 7. Deposited CASARM VX Droplet Volume and Mass and Corresponding Masses of VX and EMPA Remaining after DCA Experiments (20 h after Contamination)
Performed at 40 and 60 °C

Temperature (°C)	Initial Droplet Volume (μL)	VX Mass Delivered (mg)	VX Mass Remaining (mg)	EMPA Mass Remaining (mg)	Fraction of VX Mass Remaining
40	2.00 ± 0.04	1.97 ± 0.04	0.928 ± 0.094	0.340 ± 0.011	0.47 ± 0.039
60	2.11 ± 0.10	2.07 ± 0.09	0.010 ± 0.0076	0.577 ± 0.034	0.005 ± 0.004

The final volume of the droplet for each DCA experiment was known, but the corresponding mass was unknown due to incomplete knowledge of the mixture composition. The masses of VX and EMPA were known for each case, and thus the final droplet mass, m_d , can be written as:

$$m_d = \rho_d V_d = m_{\text{VX}} + m_{\text{EMPA}} + m_{\text{other}} \quad (15)$$

where

ρ_d is mass density of droplet at end of DCA experiment (kg m^{-3}); and

m_{other} is mass of species other than VX and EMPA in droplet (mg).

Although the exact droplet density, ρ_d , was unknown, judicious bounds were put on its value to place corresponding bounds on m_{other} . Of the other species expected to be in the mixture, VX-pyro had the highest density at 1.18 g/cm^3 , and VX-thiol had the lowest density at 0.883 g/cm^3 . Using these values to place bounds on the average density of species other than VX and EMPA in the final droplet, the mixture density can be estimated using the following mass weighted equation:

$$\frac{1}{\rho_d} = \frac{m_{\text{VX}}}{m_d} \frac{1}{\rho_{\text{VX}}} + \frac{m_{\text{EMPA}}}{m_d} \frac{1}{\rho_{\text{EMPA}}} + \frac{m_{\text{other}}}{m_d} \frac{1}{\rho_{\text{other}}} \quad (16)$$

An iterative procedure was used to compute m_{other} from eqs 15 and 16, and for the 40°C test, yielded $0.072 \text{ mg} < m_{\text{other}} < 0.189 \text{ mg}$, whereas for the 60°C test, $0.179 \text{ mg} < m_{\text{other}} < 0.242 \text{ mg}$. Based on the VX degradation mechanism presented in eqs 1–4, it was expected that this mass primarily consisted of VX-pyro, VX-thiol, VX-disulfide, and water in an unknown ratio.

3.4 DCA Results for VX/EMPA Mixtures

The effect of the initial amount of EMPA in the VX droplet was studied in a controlled manner by creating the following two mixtures of CASARM VX and EMPA: (1) a 90/10 v/v VX/EMPA mixture and (2) a 95/5 v/v VX/EMPA mixture. For each of these mixtures, DCA experiments were carried out using a $2 \mu\text{L}$ droplet at temperatures of 40°C and 60°C . The evolution of the droplet volume and contact angle for both mixtures is shown in Figure 9. First, there appeared to be little difference in the droplet volume or contact angle between the two mixture compositions at the same temperature. Qualitatively, the behavior of the droplet evaporation was similar to that observed for high-purity VX (Figure 6a) in that the evaporation rate was divided into two regimes. For the 40°C and 60°C tests, the first regime for the VX/EMPA mixtures displayed a faster evaporation rate ($\sim 0.11 \mu\text{L/h}$ at 40°C and $\sim 0.47 \mu\text{L/h}$ at 60°C) compared with that for the high-purity VX ($\sim 0.06 \mu\text{L/h}$ at 40°C and $\sim 0.25 \mu\text{L/h}$ at 60°C). In addition, the time at which the transition to the second regime occurred was earlier for the VX/EMPA mixtures ($\sim 5 \text{ h}$ at 40°C and $\sim 2 \text{ h}$ at 60°C) compared with the high-purity VX

(11 h at 40 °C and ~5 h at 60 °C). Furthermore, the transition between evaporation rate regimes at 40 °C for the VX/EMPA mixtures appeared to be much more gradual than the transition for the high-purity VX. The evolution of the contact angle for the VX/EMPA mixtures was similar to that that for high-purity VX, but like the droplet volumes, the transitions occurred earlier and at a faster rate.

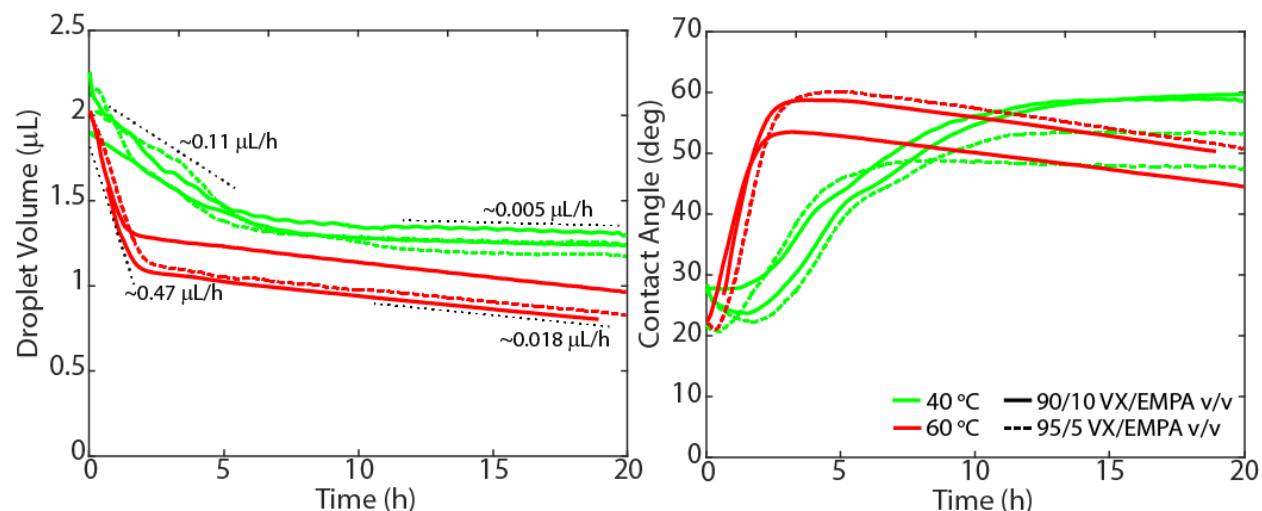


Figure 9. Evolution of (a) droplet volume and (b) contact angle for the initial ~2 μL droplets of a 90/10 v/v VX/EMPA mixture (solid lines) and a 95/5 v/v VX/EMPA mixture (dashed lines) on a borosilicate glass substrate at temperatures of 40 °C (green line) and 60 °C (red line). Dotted black lines and corresponding annotations indicate approximate droplet evaporation rates at different time intervals during the experiment.

Chemical analysis was performed to determine the amounts of VX, EMPA, and EA 2192 remaining in the droplets after the 40 and 60 °C DCA experiments. The initial deposited droplet volume and VX mass for each of these experiments are shown in Table 8, along with the VX and EMPA mass remaining after the DCA experiment. It was determined that the mass of EA 2192 was less than 1% of the mass of VX and EMPA in the mixture.

Table 8. Deposited Droplet Volume and VX Mass and Corresponding Masses of VX and EMPA Remaining after DCA Experiments Performed at 40 and 60 °C Using 95/5 and 90/10 v/v VX/EMPA Mixtures

Temperature (°C)	VX/EMPA (v/v)	Initial Droplet Volume (μL)	VX Mass Delivered (mg)	VX Mass Remaining (mg)	EMPA Mass Remaining (mg)	Fraction of VX Mass Remaining
40	95/5	2.05	1.946	0.1102	0.9733	0.057
	90/10	2.05	1.889	0.1160	0.9220	0.061
60	95/5	2.02	1.917	0.0141	0.7700	0.007
	90/10	1.99	1.833	0.0150	0.7258	0.008

Using the same method as that used to place bounds on the CASARM VX droplet density after the DCA experiment (Section 3.3), an iterative procedure was used to compute m_{other} from eqs 15 and 16. For the 40 °C test, $0.120 \text{ mg} < m_{\text{other}} < 0.236 \text{ mg}$, whereas for the 60 °C test, $0.032 \text{ mg} < m_{\text{other}} < 0.143 \text{ mg}$. Based on the VX degradation mechanism presented in eqs 1–4, this mass was expected to primarily consist of VX-pyro, VX-thiol, VX-disulfide, and water in an unknown ratio.

3.5 Contact Angle Results Summary

The contact angle data provide several indications of droplet behavior and evolution over time, including when the evaporation rate changed from higher to lower rates and when there was a chemical change (indicated by the contact angle). The summary of observations at 60 °C is provided in Table 9.

Table 9. Contact Angle Summary for VX and Related Byproducts at 60 °C

Liquid	Report Section	Transition Time (h)	Evaporation Rate ($\mu\text{L/h}$)		Contact Angle (deg)	
			Initial	Final	Initial	Final
CASARM VX	3.3	~4	0.11	0.01	~20	~50
High-purity VX	3.1	~5	0.25	0.009	32	57
VX/EMPA mixtures	3.4	~2	0.47	0.018	~20	~50
VX-disulfide	3.2	N/A	0.008	0.008	12	12
EMPA	3.2	N/A	0.05	0.05	57	32
VX-pyro	3.2	N/A	0.05	0.05	57	32

N/A, not applicable.

3.6 Phase-Separation Experiments

Figure 10 shows that a mixture of equal parts EMPA and VX-disulfide are immiscible, which provides evidence that a similar phase separation could occur in the sessile droplet.

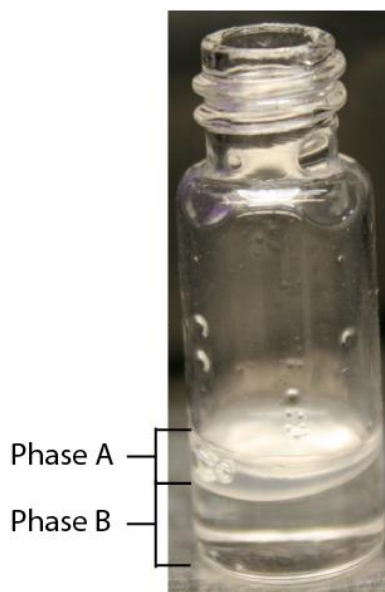


Figure 10. Mixture of EMPA and VX-disulfide vigorously mixed in a vial and allowed to settle.

3.7 Vial Reactor Experiments under Various Environmental Conditions

The influence of oxygen and water vapor in the surrounding atmosphere on the final droplet composition was determined according to the procedure in Section 2.6. The quantities of VX, EMPA, and EA 2192 remaining after each of the 24 h vial reactor experiments for an initial nominal 2 μL high-purity VX droplet at 60 $^{\circ}\text{C}$ are summarized in Table 10, along with the dose-confirmation samples.

Table 10. Molar Amounts of VX, EMPA, and EA 2192 Remaining from an Initial Nominal 2 μL Droplet of CASARM VX in a Sealed Vial at 60 $^{\circ}\text{C}$ for 24 h under Various Headspace Conditions

Parameter	Dose-Confirmation Samples	Environmental Condition				
		Dry Air	Dry Argon	Ambient Air	Humidified Air	Humidified Argon
VX (μmol)	7.05 ± 0.11	3.13 ± 0.59	2.62 ± 0.39	0.40 ± 0.14	0.03 ± 0.0016	0.04 ± 0.01
EMPA (μmol)	0.99 ± 0.03	1.35 ± 0.33	1.91 ± 0.32	4.71 ± 0.71	8.15 ± 0.15	8.39 ± 0.48
EA 2192 (μmol)	0.015 ± 0.0004	0.007 ± 0.005	0.013 ± 0.002	0.014 ± 0.0037	0.11 ± 0.046	0.094 ± 0.018
Total (μmol)	8.06 ± 0.14	4.49 ± 0.93	4.54 ± 0.72	5.13 ± 0.86	8.29 ± 0.15	8.53 ± 0.51
VX fractional conversion	N/A	0.56	0.63	0.95	1.0	0.99

The results indicate that for the humidified argon and humidified air tests, the conversion of VX was complete, and EMPA was the primary phosphorus-containing byproduct. Molar balance was observed in these tests by comparing the total molar amount to that of the dose-confirmation sample. For the humidified atmosphere samples, measurable amounts of EA 2192 that were relative to the dose-confirmation samples were observed. All of these observations are consistent with those of Brevett et al. for the degradation of VX on wet sand.³

For the case of ambient air, the VX fractional conversion was about 95%, and EMPA was the primary phosphorus-containing byproduct. Molar balance was not observed in this case when comparing the total molar amount to that of the dose-confirmation sample. This indicated that there were other phosphorus-containing byproducts in the droplet at the end of the experiment. Based on the reaction mechanism, the most obvious candidate for this byproduct was VX-pyro. This was corroborated by observations of VX degradation on dry sand at 50 °C by Brevett et al.,³ in which measurable quantities of VX-pyro were observed long after the VX had completely disappeared.

For the dry air and argon tests, the VX fractional conversions were 0.56 and 0.63, respectively. Assuming that water had been completely eliminated from the system, VX degradation could have only proceeded by reaction 2 in the mechanism (eq 2) using the EMPA available in the initial droplet and generating VX-pyro and VX-thiol. In the absence of water, the VX-pyro could not have been converted to EMPA via reaction 3 (eq 3); therefore, the autocatalytic mechanism was disrupted, and VX degradation was significantly slowed. Similar to the test for ambient air, the apparent lack of molar balance as compared with the dose-confirmation sample was most likely accounted for by the VX-pyro in the mixture.

Also note that the final amounts were approximately equivalent whether argon or air was used (for both dry and humid tests), which indicated that atmospheric oxygen does not play a significant role in VX degradation.

Figure 11 shows the amounts of VX and VX-disulfide normalized to the corresponding arbitrary values in the dose-confirmation samples as described in Section 2.2.

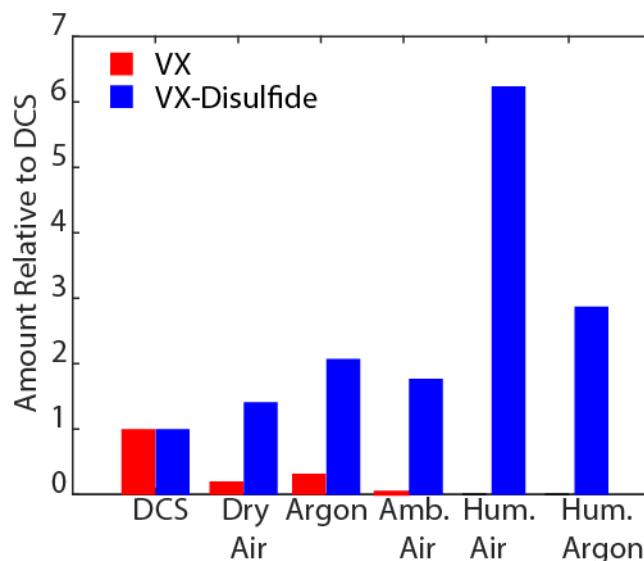


Figure 11. Relative amounts of VX and VX-disulfide remaining after 24 h vial reactor experiments at 60 °C, in various atmospheric conditions, with the amounts in the initial droplet (dose-confirmation sample) as the reference.

3.8 Summary of Key Experimental Results

The following summarizes the major findings from the contact angle and vial reactor experiments for each type of VX used:

- The DCA experiments showed two distinct regimes of evaporation rate and contact angle for a sessile droplet of high-purity VX at temperatures above 40 °C: (1) An initial regime with a constant evaporation rate and a contact angle between 20 and 30°, followed by a sharp transition to (2) a second regime with a much slower evaporation rate (nearly nonvolatile) and a contact angle between 50 and 60°.
- Corresponding vial reactor experiments and chemical analyses showed that the degradation byproducts EMPA and VX-disulfide were produced and that VX-pyro was also likely produced; all of these are known byproducts from the autocatalytic hydrolysis of VX.
- The evaporation rate of high-purity VX at 60 °C in the second regime closely agreed with that of VX-disulfide at 60 °C.
- The contact angle of high-purity VX at 60 °C closely agreed with those of EMPA and VX-pyro.

These observations suggested that the sessile droplet of high-purity VX underwent a known autocatalytic degradation process, and the sharp transition in evaporation and contact angle corresponded to a significant change in chemical composition. Here, the

droplet core consisted of a mixture of hydrophilic components, EMPA and VX-pyro, which defined the contact angle, and a shell that consisted of the hydrophobic component VX-disulfide.

In DCA and vial reactor experiments, the initial amount of EMPA in the droplet and the available humidity in the surrounding atmosphere were important quantities for the degradation process. This was highlighted as follows:

- CASARM VX had no initial EMPA in the droplet, and the evaporation and degradation processes were noticeably slower;
- additional EMPA increased the rates of evaporation and degradation; and
- high humidity in the surrounding atmosphere led to a faster degradation of VX, whereas the conversion of VX was incomplete in dry conditions.

These observations are commensurate with the previously reported autocatalytic degradation mechanism given for VX.

4. COMPUTATIONAL RESULTS

4.1 Estimation of Gas-Phase Diffusivities

Diffusivities of VX and its degradation byproducts in the gas phase, $D_{i,g}$, were estimated using the Wilke–Lee correlation.¹⁰

$$D_{i,g} = \frac{B'M_r^{0.5}T^{1.5}}{p\sigma_{ia}^2\Omega} \quad (17)$$

$$M_r = \frac{M_i + M_a}{M_i M_a} \quad (18)$$

$$B' = 0.00217 - 5 \times 10^{-4} \left(\frac{1}{M_i} + \frac{1}{M_a} \right)^{0.5} \quad (19)$$

$$\Omega = \frac{a}{(T^*)^b} + \frac{c}{\exp(dT^*)} + \frac{e}{\exp(fT^*)} + \frac{g}{\exp(hT^*)} \quad (20)$$

$$T^* = \frac{T}{1.15T_b} \quad (21)$$

where

- B is an empirical constant;
- T is air temperature (K);
- p is air pressure (atm);
- M_r is reduced molecular mass;
- M_a is mean molecular mass of air (g/mol);
- M_i is molecular mass of species i (g/mol);
- σ_{ia} is arithmetic mean of species i and nitrogen molecular diameters;
- T_b is normal boiling temperature of species i (K); and
- $a-h$ are constants.

The constants in eq 20 are given by $a = 1.0606$, $b = 0.1561$, $c = 0.193$, $d = 0.47635$, $e = 1.03587$, $f = 1.52996$, $g = 1.76474$, and $h = 3.89411$. The resulting values for the diffusivities at 60 °C are provided in Table 11.

Table 11. Diffusivities of VX and Degradation Byproducts in Air at 60 °C as Computed by the Wilke–Lee Correlation

Chemical	Diffusivity at 60 °C (m ² /s)
VX	5.56×10^{-6}
EMPA	9.27×10^{-6}
VX-pyro	6.52×10^{-6}
VX-thiol	7.19×10^{-6}
VX-disulfide	4.79×10^{-6}
Water	2.82×10^{-5}

4.2 Estimation of Vapor Pressures

For VX and water, previously developed Antoine coefficients were used to estimate vapor pressures. The vapor pressure (Pa) of VX as a function of temperature (K) is given by⁵

$$\ln p_{\text{VX}}^{\text{vap}} = 23.725 - \frac{6154.9}{T - 60.165} \quad (22)$$

The vapor pressure (Pa) of water as a function of temperature (K) is given as¹¹

$$\ln p_w^{\text{vap}} = 23.1963 - \frac{3816.44}{T - 46.143} \quad (23)$$

The vapor pressure of VX-thiol at 25 °C, $p_{\text{RSH}}^{\text{vap},298\text{K}}$, was estimated to be 67 Pa from the Advanced Chemistry Development (ACD/Labs; Toronto, Canada) PhysChem Module¹² and 78 Pa from the U.S. Environmental Protection Agency Estimation Programs Interface Suite (Washington, DC).⁴ The average of these two values, 72.5 Pa, and the Clausius–Clapeyron equation were used to extrapolate and find the corresponding vapor pressure at 60 °C.

$$\ln \frac{p_{\text{RSH}}^{\text{vap}}}{p_{\text{RSH}}^{\text{vap},298\text{K}}} = \frac{\Delta H_{\text{RSH}}^{\text{vap}}}{R} \left(\frac{1}{298} - \frac{1}{T} \right) \quad (24)$$

where

$\Delta H_{\text{RSH}}^{\text{vap}}$ is enthalpy of vaporization of VX-thiol at 25 °C (J/mol); and
 R is universal ideal gas constant (J mol⁻¹ K⁻¹).

The enthalpy of vaporization of VX-thiol at standard conditions was found from the ACD/Labs PhysChem Module to be 42.752 kJ/mol. This gave an estimated vapor pressure of 444 Pa for VX-thiol at 60 °C.

To estimate the vapor pressures for the VX degradation byproducts EMPA, VX-pyro, and VX-disulfide, the DCA experiments on these pure components at 60 °C (Section 3.2) along with the corresponding estimates of the gas-phase diffusivities at 60 °C (Section 4.1) were used. To do this, a COMSOL model was used to simulate the evaporation of each of these pure components using (1) eqs 5–9 in the liquid phase, assuming that the reaction rate constants k_i equals 0 for all i ; (2) eq 10 in the gas phase; and (3) the diffusivities in Table 11. The vapor pressures of the pure components were adjusted to provide the best fit to the corresponding DCA data at 60 °C (Figure 12). The vapor pressures of each of the species considered in this study are listed in Table 2.

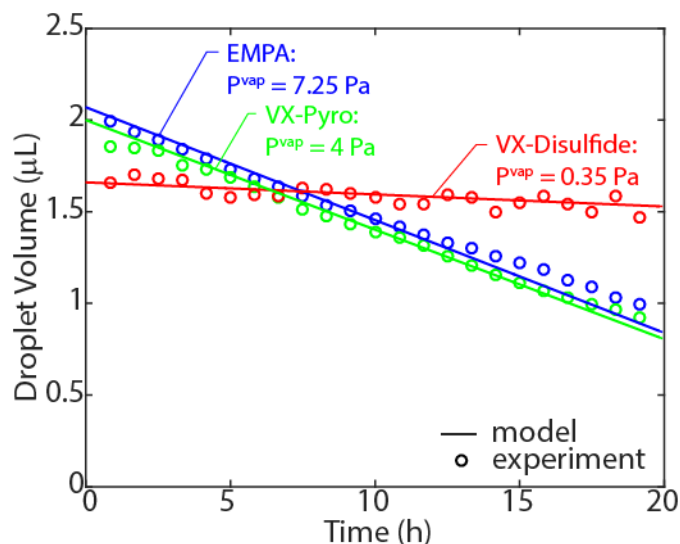


Figure 12. Fit of COMSOL evaporation models (solid lines) of EMPA (blue line), VX-pyro (green line), and VX-disulfide (red line) to experimental DCA data at 60 °C (open circles) by adjusting corresponding vapor pressures in the model.

4.3 Degradation and Evaporation for Fixed Droplet Geometry

Simulations of the evaporation and degradation of a 2 μL droplet at 60 °C for different values of the initial composition (100% VX, 95% VX/5% EMPA, 90% VX/10% EMPA, and 85% VX/15% EMPA by moles) were performed with the COMSOL software according to the equations presented in Section 2.7. In addition, because no kinetic data was available for the dimerization of VX-thiol to VX-disulfide (i.e., rate constant, k_4), a range of values was studied ($k_4 = 100, 500, 1000$, and $5000 \text{ mol}^{-1} \text{ s}^{-1}$).

The model-predicted evolution of droplet volume for an initial composition of 85% VX/15% EMPA is shown in Figure 13 for all values of the VX-thiol dimerization rate constant, k_4 . The predicted volume evolution did not significantly differ among the different starting compositions. Also shown is the experimentally observed evolution of droplet volume for approximately the same starting composition. None of the model-predicted droplet evolution curves reproduced the experimentally observed curve. There were several factors that could have accounted for this:

1. The kinetics used in the model implicitly accounted for water in the rate constants; therefore, if the water content in the experiments differed from the water content in the kinetic experiments, the evolution of the system could differ.
2. The model assumes that the liquid mixture behaves as an ideal solution, which is unlikely to be the case. In reality, the vapor pressure of each

component could be a nonlinear function of composition, which would have a strong influence over the evaporation rate.

3. The model does not account for possible phase separation of the components at a critical solution composition, which would exhibit a sharp transition in the evaporation rate as was observed experimentally.

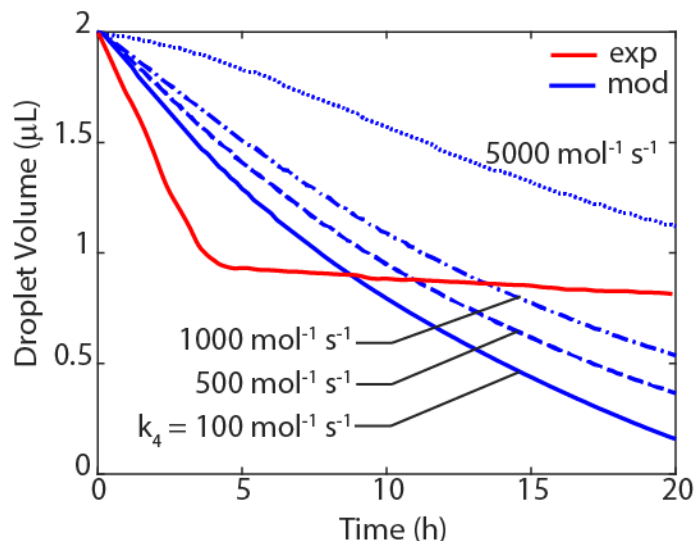


Figure 13. Simulated evolution of droplet volume for an initially 2 μL droplet containing 85% VX and 15% EMPA by moles at 60 $^{\circ}\text{C}$ (blue line) for different values of rate constant, $k_4 = 100 \text{ mol}^{-1} \text{ s}^{-1}$ (solid blue line), $500 \text{ mol}^{-1} \text{ s}^{-1}$ (dashed blue line), $1000 \text{ mol}^{-1} \text{ s}^{-1}$ (dash-dot blue line), and $5000 \text{ mol}^{-1} \text{ s}^{-1}$ (dotted blue line), and for comparison to corresponding experimental result (red line).

Figure 14 shows the corresponding simulated composition evolution for the 2 μL droplet (initially consisting of 85% VX/15% EMPA by moles) at 60 $^{\circ}\text{C}$. The degradation time scale of 20 h was similar to that reported by Brevett et al.³ for the degradation of VX on dry sand at 55 $^{\circ}\text{C}$. In the experiments performed by Brevett et al., more VX-pyro was produced and decayed more slowly, whereas the production of EMPA continued until 100 h after the VX was deposited on the sand. Contrast this with the predicted composition evolution in the droplet, in which the EMPA peaked at ~ 5 h and then began to decay, whereas VX-pyro peaked at about 10 h. This was likely because the VX–sand mixtures were placed in sealed tubes that limited the evaporation, whereas the simulations were conducted for an open atmosphere.

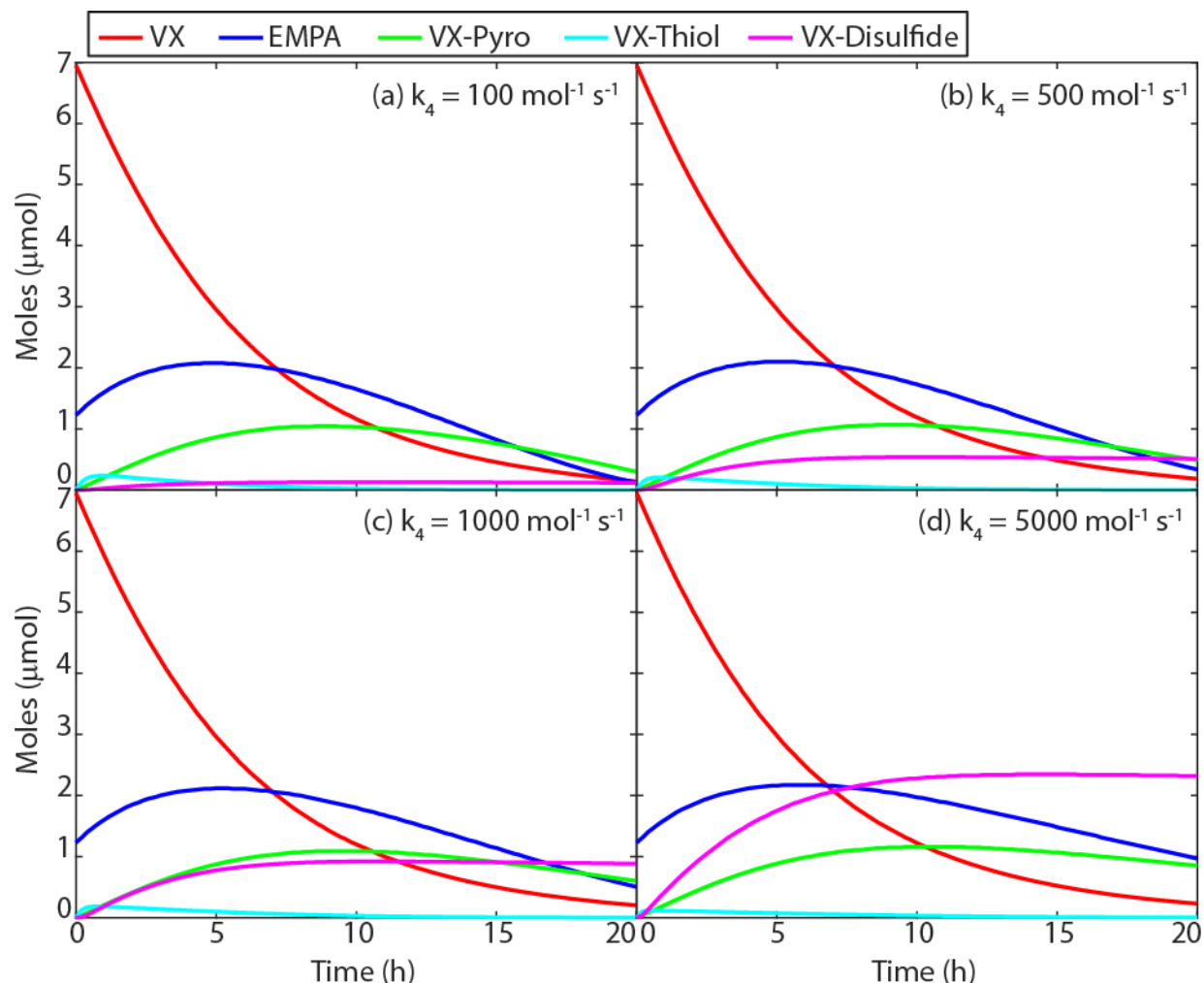


Figure 14. Simulated evolution of composition in an initial 2 μL droplet containing 85% VX and 15% EMPA by moles at 60 °C. (a) $k_4 = 100 \text{ mol}^{-1} \text{ s}^{-1}$, (b) $k_4 = 500 \text{ mol}^{-1} \text{ s}^{-1}$, (c) $k_4 = 1000 \text{ mol}^{-1} \text{ s}^{-1}$, and (d) $k_4 = 5000 \text{ mol}^{-1} \text{ s}^{-1}$. VX (red line), EMPA (blue line), VX-pyro (green line), VX-thiol (cyan line), and VX-disulfide (magenta line).

5. SUMMARY AND CONCLUSIONS

DCA experiments at elevated temperatures (40–60 °C) on borosilicate glass showed that high-purity VX underwent evaporation in two distinct rate regimes with a sharp transition between them: (1) an initial, relatively slow evaporation rate regime, followed by (2) a nearly nonvolatile regime in which the droplet evaporation was very slow and approximately equal to that of the degradation product VX-disulfide. The contact angle of high-purity VX correspondingly showed two regimes: (1) an initial regime of $\sim 20\text{--}30^\circ$ followed by (2) a transition to a contact angle of $\sim 50\text{--}60^\circ$, which closely matched the contact angle observed for the degradation products EMPA and VX-pyro.

Vial reactor experiments indicated that VX degradation occurred via the autocatalytic hydrolysis mechanism proposed by Yang et al.² and Brevett et al.,³ with EMPA as

the primary phosphorus-containing byproduct, and VX-pyro remaining when there was insufficient water to fully convert intermediate VX-pyro to EMPA. Qualitative results indicated the production of VX-disulfide.

The combined results of the DCA and vial reactor experiments indicated the likelihood that the transition between evaporation rate and contact angle regimes was caused by phase separation at a critical mixture composition. In this process, the droplet transitioned from a single-phase mixture (first regime) to a two-phase mixture (second regime) that consisted of a hydrophilic core made up of EMPA and VX-pyro and surrounded by a hydrophobic core that contained VX-disulfide.

Modeling results showed that treating the VX/EMPA mixture as an ideal liquid solution could not reproduce the experimentally observed droplet volume evolution. However, non-ideal solution effects could not be ruled out. In other words, phase separation is not the only possible explanation for the observed transition between evaporation rate and contact angle regimes. The mixture of VX and its byproducts could show a highly nonlinear relationship between vapor pressure and surface tension as a function of composition. However, this appears to be the less likely scenario based on current evidence.

To definitively show that a phase-separation process was occurring in the evaporation and degradation process of VX at an elevated temperature, additional information is needed. The simplest way this could be accomplished would be to employ an optical technique during the DCA experiments that would enable differentiation between phases to confirm that the droplet separates into a core and shell, as suspected. Another, far more laborious method would be to develop a rudimentary phase diagram of VX and its degradation byproducts by creating mixtures of known composition that are informed by the kinetic model to identify transitions between single- and two-phase regions, as a function of composition. Although more laborious, this would also enable modeling of the phase-separation process.

This work also illustrates the difficulty in modeling the contamination and decontamination of materials exposed to VX at elevated temperature, as is required in the Decon SPM. This model simulates the contamination of materials from a single sessile droplet of CWA and the subsequent decontamination process and provides estimates for post-decontamination hazards. It is clear that the severity of the post-decontamination hazards can be greatly influenced by the initial contamination process. Given the complexity of the VX evaporation and degradation process, as shown by this work, and the fact that the Decon SPM must also simulate the sorption of species from the liquid droplet into the bulk of materials (e.g., paint coatings), there can be a great deal of uncertainty in predicting the hazards for VX at elevated temperatures. The absorption of degradation byproducts into materials (i.e., a multicomponent diffusion process) must be considered, along with the (possibly changing) relative rates of absorption, evaporation, and degradation. Accurate prediction of all of these processes requires a good deal more experimental work, analysis, and modeling.

Blank

LITERATURE CITED

1. Engleman, A.; Dennis, R.; Lull, D.; Hedley, W.H.; Long, R.L.; Paullin, K.A. *Dissemination of Inhalable Aerosols*; GCA Corporation: Bedford, MA, 1972.
2. Yang, Y.C.; Szafraniec, L.L.; Beaudry, W.T.; Rohrbaugh, D.K.; Procell, L.R.; Samuel, J.B. Autocatalytic Hydrolysis of V-Type Nerve Agents. *J. Org. Chem.* **1996**, *61* (24), 8407–8413.
3. Brevett, C.A.S.; Sumpter, K.B.; Pence, J.; Nickol, R.G.; King, B.E.; Giannaras, C.V.; Durst, H.D. Evaporation and Degradation of VX on Silica Sand. *J. Phys. Chem. C* **2009**, *113* (16), 6622–6633.
4. EPA. *Estimation Programs Interface (EPI) Suite*; U.S. Environmental Protection Agency: Washington, DC, 2017.
5. Tevault, D.E.; Brozena, A.; Buchanan, J.H.; Abercrombie-Thomas, P.L.; Buettner, L.C. Thermophysical Properties of VX and RVX. *J. Chem. Eng. Data* **2012**, *57* (7), 1970–1977.
6. Willis, M.; Mantooth, B.; Hover, M.; Lalain, T. *Experimental and Computational Methodology for the Estimation of Mass Transport Parameter Values of Chemical Warfare Agents in Military Relevant Substrates*; ECBC-TR-890; U.S. Army Edgewood Chemical Biological Center: Aberdeen Proving Ground, MD, 2011. UNCLASSIFIED Report (ADB379904).
7. *COMSOL Multiphysics User's Guide*, version 5.1; COMSOL, Inc.: Burlington, MA, 2015.
8. Karpitschka, S.; Liebig, F.; Riegler, H. Marangoni Contraction of Evaporating Sessile Droplets of Binary Mixtures. *Langmuir* **2017**, *33* (19), 4682–4687.
9. Diddens, C.; Kuerten, J.G.M.; van der Geld, C.W.M.; Wijshoff, H.M.A. Modeling the Evaporation of Sessile Multi-Component Droplets. *J. Colloid Interface Sci.* **2017**, *487*, 426–436.
10. Perry, R.H.; Green, D.W. *Perry's Chemical Engineers' Handbook*, 7th ed.; Perry, R.H.; Green, D.W., Eds; McGraw-Hill Professional: New York, 1997.
11. *CRC Handbook of Tables for Applied Engineering Science*, 2nd ed.; Bolz, R.E., Tuve, G.L., Eds.; CRC Press: Boca Raton, FL 1976.
12. *ACD/Labs Physchem Profiler*, Advanced Chemistry Development, Inc.: Toronto, Ontario, Canada, 2015.

Blank

ACRONYMS AND ABBREVIATIONS

ACD/Labs	Advanced Chemistry Development Laboratories
ATR	attenuated total reflection
CASARM	Chemical Agent Standard Analytical Reference Material
CWA	chemical warfare agent
DCA	dynamic contact angle
Decon SPM	Decontamination System Performance Model
ECBC	U.S. Army Edgewood Chemical Biological Center
EMPA	ethyl methylphosphonic acid
FTIR	Fourier transform infrared
GC	gas chromatography
IPA	isopropyl alcohol
LC	liquid chromatography
Log $K_{o/w}$	log octanol–water partition coefficient
MPA	mobile phase A
MPB	mobile phase B
MRM	multiple-reaction method
MS	mass spectroscopy
MS/MS	tandem mass spectroscopy
NMR	nuclear magnetic resonance
ODE	ordinary differential equations
RSH	VX-thiol
RSSR	VX-disulfide
VLE	vapor–liquid equilibrium
VX	2-(diisopropylamino)ethyl- <i>O</i> -ethyl methylphosphonothioate
VX-pyro	VX byproduct

Blank

APPENDIX AGENT PURITY CERTIFICATES

A-1. Composition Report for High-Purity VX for the Agent in 2008

Lot # VX-U-1244-CTF-N

ADDITIONAL ANALYTICAL INFORMATION (CONT'D)

d. NMR; analyzed 21 November 2011

¹H, ¹³C and ³¹P NMR spectra are consistent with the following interpretation; analyzed using a semi-quantitative method because no internal/external standards were used. Method reproducibility is approximately ± 0.5 mole % and method detection limit is approximately ± 0.04%.

Compound	Mole %	Weight %
O-Ethyl S-2-diisopropylaminoethyl methylphosphonothiolate (VX), CH ₃ P(O)(OCH ₂ CH ₃)(SR)	95.9	96.5
Bis(S-2-[Diisopropylamino]ethyl) methylphosphonodithiolate (bis), CH ₃ P(O)(SR) ₂	(0.03)	(0.04)
Diethyl dimethyldiphosphonate (VX pyro), CH ₃ P(O)(OCH ₂ CH ₃)OP(O)(CH ₃)(OCH ₂ CH ₃)	0.15	0.13
2-Diisopropylaminoethyl ethyl methylphosphonite (QL), CH ₃ P(OCH ₂ CH ₃)(OR)	0.89	0.79
Bis(Diisopropylaminoethyl) methylphosphonite (LT), CH ₃ P(OR) ₂	(0.02)	(0.03)
Diethyl methylphosphonite (TR), CH ₃ P(OEt) ₂	(0.008)	(0.004)
O,O-Diethyl methylphosphonothionate (TRS), CH ₃ P(S)(OCH ₂ CH ₃) ₂	0.39	0.25
O-2-Diisopropylaminoethyl O-ethyl methylphosphonothionate (CV), CH ₃ P(S)(OR)(OCH ₂ CH ₃)	0.16	0.16
O-(2-Diisopropylaminoethyl) methylphosphinic acid (QA), CH ₃ P(O)(OR)H	0.35	0.27
O-Ethyl methylphosphinic acid (YL), CH ₃ P(O)(OCH ₂ CH ₃)H	0.33	0.14
Bis(2-diisopropylaminoethyl) methylphosphonate (LTO), CH ₃ P(O)(OR) ₂	0.05	0.07
2-Diisopropylaminoethyl ethyl methylphosphonate (QLO), CH ₃ P(O)(OR)(OCH ₂ CH ₃)	0.77	0.73
Diethyl methylphosphonate (TRO, DEMP), CH ₃ P(O)(OCH ₂ CH ₃) ₂	0.10	0.06
O-Ethyl methylphosphonothioic acid (EMPSH), CH ₃ P(S)(OCH ₂ CH ₃)(OH)	(0.02)	(0.01)
Ethyl methylphosphonic acid (EMPA), CH ₃ P(O)(OCH ₂ CH ₃)(OH)	(0.01)	(0.005)
CH ₃ P(S)(OCH ₂ CH ₃)OP(O)(CH ₃)(OCH ₂ CH ₃) (Unsym Pyro)	(0.02)	(0.02)
CH ₃ P(S)(OCH ₂ CH ₃)SP(S)(CH ₃)(OCH ₂ CH ₃) (PSP pyro)	(0.06)	(0.06)
Other compounds δ 69-115, P=S type	0.07	0.07
Other compounds δ 37-69, R'P(O)(SR'')-, (R'O) ₃ P(S), and R' ₂ P(O)- types	0.59	0.60
Other compounds δ 19-37, phosphonic acids/esters	0.07	0.07
Other compounds δ 0-19, other acids	(0.03)	(0.03)
Other compounds δ 130-160 area, PIII compounds	0.04	0.04

R = CH₂CH₂N[CH(CH₃)₂]₂

R' & R'' are unknown

() = at or below MDL

Date of Issue **MAR 30 2012**

Composition Report for High-Purity VX for the Agent in 2008

AMSRD-ECB-CB-SQ

APR 30 2008

MEMORANDUM FOR RECORD

SUBJECT: Information on the Analysis of VX-U-7011-CTF-N

1. VX-U-7011-CTF-N is **NOT A CASARM**.

2. The following information is provided for information purposes only.
³¹P and ¹³C NMR spectra are consistent with the following interpretation; analyzed on 21 January 2007. Please note that the reported weight % values were derived from laboratory reported mole % values (± 0.04%) that are based on mole ratios and are not absolute.

<u>Compound</u>	<u>Weight %</u>
O-Ethyl S-2-diisopropylaminoethyl methylphosphonothiolate (VX), CH ₃ P(O)(OCH ₂ CH ₃)(SR)	89.5
Bis(S-2-[Diisopropylamino]ethyl) methylphosphonodithiolate (bis), CH ₃ P(O)(SR) ₂	1.33
Diethyl dimethyldiphosphonate (VX pyro), CH ₃ P(O)(OCH ₂ CH ₃)OP(O)(CH ₃)(OCH ₂ CH ₃)	0.95
Diisopropylaminoethyl ethyl methylphosphonite (QL), CH ₃ P(OCH ₂ CH ₃)(OR)	ND
Bis(Diisopropylaminoethyl) methylphosphonite (LT), CH ₃ P(OR) ₂	ND
Diethyl methylphosphonite (TR), CH ₃ P(OEt) ₂	ND
O,O-Diethyl methylphosphonothiolate (TRS), CH ₃ P(S)(OCH ₂ CH ₃) ₂	0.45
O-Diisopropylaminoethyl O-ethyl methylphosphonothiolate (CV), CH ₃ P(S)(OR)(OCH ₂ CH ₃)	4.63
Diisopropylaminoethyl methylphosphonite (QA), CH ₃ P(O)(OR)H	(0.02)
Ethyl methylphosphonite (YL), CH ₃ P(O)(OCH ₂ CH ₃)H	(0.02)
Bis(Diisopropylaminoethyl) methylphosphonate (LTO), CH ₃ P(O)(OR) ₂	(0.03)
Diisopropylaminoethyl ethyl methylphosphonate (QLO), CH ₃ P(O)(OR)(OCH ₂ CH ₃)	0.94
Diethyl methylphosphonate (TRO, DEMP), CH ₃ P(O)(OCH ₂ CH ₃) ₂	0.08
O-Ethyl methylphosphonothioic acid (EMPSH), CH ₃ P(S)(OCH ₂ CH ₃)(OH)	ND
Ethyl methylphosphonic acid (EMPA), CH ₃ P(O)(OCH ₂ CH ₃)(OH)	0.03
CH ₃ P(S)(OCH ₂ CH ₃)OP(O)(CH ₃)(OCH ₂ CH ₃) (Unsym Pyro)	0.25
CH ₃ P(S)(OCH ₂ CH ₃)SP(S)(CH ₃)(OCH ₂ CH ₃) (PSP pyro)	0.08
Diisopropylaminoethane thiol (RSH)	0.92
Diisopropylaminoethane disulfide (RSSR)	ND
Other compounds δ 0-39, acids/esters	0.07

DISTRIBUTION LIST

The following individuals and organizations were provided with one Adobe portable document format (pdf) electronic version of this report:

U.S. Army Edgewood Chemical
Biological Center (ECBC)
RDCB-DRP-D

ATTN: Varady, M.
Mantooth, B.
Procell, L.
Morrissey, K.

G-3 History Office
U.S. Army RDECOM
ATTN: Smart, J.

ECBC Technical Library
RDCB-DRB-BL
ATTN: Foppiano, S.
Stein, J.

Defense Threat Reduction Agency
J9-CBS

ATTN: Graziano, A.
Roberts, M.
Hannan, J.
Lowenstein, E.

Office of the Chief Counsel
AMSRD-CC
ATTN: Upchurch, V.

Department of Homeland Security
RDCB-PI-CSAC
ATTN: Negron, A.
DHS-S&T-RDP-CSAC
ATTN: Strang, P.

ECBC Rock Island
RDCB-DES
ATTN: Lee, K.
RDCB-DEM
ATTN: Grodecki, J.

Defense Technical Information Center
ATTN: DTIC OA

